

Technical University of Munich
Department of Physics
Chair of Dark Matter, E47



Master's Thesis in Physics

Investigation of an ASIC-based readout system for LEGEND and implementation of the LQ cut into JULEANA

Andreas Gieb

26. Juli 2024



First Examiner (Supervisor): Prof. Dr. Susanne Mertens
Second Examiner: Prof. Dr. Lothar Oberauer

Abstract

The search for the neutrinoless double beta decay ($0\nu\beta\beta$) is one of the most interesting topics in modern physics. Its discovery would mean that neutrinos are Majorana particles i.e. their own anti particles. The violation of lepton number conservation would open a new field beyond the Standard Model that could lead to an explanation for the matter-antimatter asymmetry. Additionally, it would be possible to extract information about the neutrino mass.

One of the most promising experiments searching for this rare decay is the Large Enriched Germanium Detector Experiment for $0\nu\beta\beta$ (LEGEND) searching for the decay of ^{76}Ge . The experiment undergoes a two-staged approach with the first phase LEGEND-200 currently taking data in the underground facilities at the Laboratori Nazionali del Gran Sasso (LNGS) with up to 200kg of ^{76}Ge -enriched Detectors. The second phase LEGEND-1000 plans to deploy 1000kg and measure over 10 years to reach an exposure of 10 t yr, aiming to reach a half life discovery sensitivity of $1.3 \cdot 10^{28}\text{yr}$ by achieving a background index of $1 \cdot 10^{-5} \frac{\text{cts}}{\text{keV}\cdot\text{kg}\cdot\text{yr}}$. With this the inverted ordering regime for a majorana neutrino will be covered.

To reach the low backgrounds needed for the experiment, different layers of shielding are utilized. These include the mountain overburden of the Gran Sasso massive, a muon veto, and the Liquid Argon Instrumentation. An advantage of germanium detectors is their capability to reject background events from signal events through the process of pulse shape discrimination. One effective method for rejecting background events is the Late Charge (LQ) cut, which is particularly sensitive to alpha events on the detector's surface. This work will highlight the implementation of this cut into the JULEANA analysis framework.

To ensure the success of LEGEND-1000, various strategies need to be implemented to further improve the already small background index required in the LEGEND-200 phase of the experiment. One of these background mitigation strategies involves the use of an application-specific integrated circuit (ASIC) as a signal amplifier, located near the detector. With this approach, a reduction in background is achievable while maintaining good energy resolution, energy linearity, and pulse shape discrimination performance. This work provides a first glimpse into the realization of this idea through the analysis of the LUIGI ASIC's first iteration.

Contents

1	Neutrino Physics	1
1.1	History of neutrinos	1
1.2	Neutrino oscillations and neutrino masses	2
1.2.1	Experimental discovery	2
1.2.2	Theory	3
1.3	Double Beta Decay	4
2	Semiconductor Detectors	10
2.1	Properties of semiconductors	10
2.2	Detector working principle	12
2.3	Germanium detectors in LEGEND	14
2.3.1	Signal formation and weighting potential	14
2.3.2	Detector geometries	15
2.4	Interaction of particles with matter	17
2.4.1	Charged particles	17
2.4.2	Gamma radiation	18
3	The LEGEND Experiment	22
3.1	Overview	22
3.2	LEGEND-200	23
3.3	Data analysis	26
3.3.1	Energy reconstruction	27
3.3.2	Pulse Shape Discrimination	28
3.4	LEGEND-1000	29
4	Implementation of the Late Charge cut for the Juleana Analysis	33
4.1	Motivation of the LQ-cut	33
4.1.1	Surface background sources	33
4.1.2	Germanium detector surface effects	34
4.1.3	Advantages of the LQ cut	35
4.2	LQ cut implementation in JULEANA	36
4.2.1	Parameter extraction	36

4.2.2	Raw LQ corrections	36
4.2.3	Final cut estimation	38
4.2.4	Performance and conclusion	39
5	Results from the first iteration of the ASIC-based readout system LUIGI	44
5.1	Signal readout electronic for LEGEND-1000	44
5.1.1	CSA working principle	44
5.1.2	Electroic Noise	45
5.1.3	CSA in LEGEND-200	47
5.1.4	LUIGI ASIC	48
5.2	First results of the LUIGI-RF ASIC	49
5.2.1	Bench tests with the LUIGI-RF ASIC	50
5.2.2	Detector Measurements	52
5.2.3	Results of the LUIGI-RF ASIC version with an external Capacity	57
5.3	Conclusion and changes for the second version of the LUIGI ASIC . . .	58
6	Summary and outlook	62
A	JULEANA gamma peak fit shape	64

Chapter 1

Neutrino Physics

Neutrinos are among the most fascinating particles in the Standard Model of particle physics. Despite their abundance in the universe, their elusive nature and tiny mass makes them difficult to study. Currently, the exact mass of neutrinos remains one of the great mysteries in modern physics. This chapter gives in an introduction to what we already know about the neutrino and what we can still learn about it from the neutrinoless double beta decay to potentially uncover new physics beyond the Standard Model.

1.1 History of neutrinos

In the SM, neutrinos are massless, neutral leptons that can only participate through the weak interaction. The first clue for the existence of the neutrino was given by analysing the energy spectrum produced by electrons emitted through β decay. Originally it was thought that the β decay was a two body process. This would mean that the core and the emitted electron need to have the same momentum due to energy conservation which would lead to a mono-energetic peak in the energy spectrum. But the real measured spectrum show a broad energy distribution. To explain this Wolfgang Pauli postulated in 1930 a new particle which he called at that time "Neutron" [1]. This makes the β decay into a three-body process, explaining the differences in momentum due to the new particle inheriting some part of it. Only two years later Chadwick discovered the particle we today call the neutron [2, 3], the name for the particle postulated by Pauli was changed to neutrino. The β decay can be expressed by the formula:

$$(Z, A) \rightarrow (Z + 1, A) + e^- + \bar{\nu}_e \quad (1.1)$$

Here Z denotes the atomic number, A the mass number of the nucleus, e^- the electron, and $\bar{\nu}_e$ the electron antineutrino.

The neutrino was first experimentally discovered by the groups of C. L. Cowan Jr. and F. Reines in 1965 in the Savannah River experiment [4]. The main part of the project was a water tank filled with dissolved cadmium chloride (CdCl_2). The detection relied on the inverse β process, where a proton (p) and a neutrino $\bar{\nu}_e$ create a neutron (n) and an positron (e^+):



The positron produced by this interaction annihilates and creates 2 γ rays. The neutron can be captured by the Cadmium putting it into an excited state. One or more γ rays are emitted when it de-excites to its ground state. Through the observation of these gammas in coincidence Cowan and Reines were able to prove that the β beta decay took place. Reines was honoured with the Nobel prize in 1995 for his contribution in the discovery.

1.2 Neutrino oscillations and neutrino masses

In the Standard Model framework, neutrinos were long considered massless particles. However, the discovery of neutrino oscillations through experimental evidence has fundamentally challenged this view. This phenomenon expands our understanding of neutrino properties beyond the Standard Model's predictions, prompting further research into the nature of neutrinos.

1.2.1 Experimental discovery

The concept of neutrino oscillations emerged from the solar neutrino problem, where the observed number of electron neutrinos from the sun was significantly less than theoretical predictions. In 1968, Raymond Davis was the first one to find this discrepancy with the Homestake experiment [5]. The group counted the number of Argon atoms produced by inverse β decay in their experiment setup.



They observed that the count of Argon atoms was only one third of the expected number [6]. Davis' experiment was only sensitive to electron neutrinos since it relayed on the charged current. Only the later Sudbury Neutrino Observatory (SNO) gave the full verification that the electrons neutrinos from the sun changed their flavor. SNO was able to detect electron neutrinos interacting through the charged current, as well as all neutrino flavours through the neutral current. The result showed that the sum of the flux of all neutrino flavors matched the predicting flux for the electron neutrino flux coming from the sun. At the same time the measured electron neutrino flux was smaller than the expected flux [7]. That proved that the electron neutrinos changed their flavor into μ and τ neutrinos.

During the same time, Super-Kamiokande was investigating the flux of atmospheric

neutrinos reaching Earth. Through analyzing the Cerenkov light emitted by the charged leptons produced by neutrinos interactions, the direction of the neutrino was determined. The collaboration was able to prove that expected flux ratio of $\nu_\mu : \nu_e = 2 : 1$, depending on how far they traveled, changed because some of the μ neutrinos changed into τ neutrinos [8].

1.2.2 Theory

The theoretical model of Neutrino oscillations assumes that the flavor eigenstates $|\nu_l\rangle$ ($l = e, \mu, \tau$) of the neutrino are superpositions of their mass eigenstates $|\nu_i\rangle$ ($i = 1, 2, 3$). The relation between the states can be expressed by:

$$|\nu_l\rangle = \sum_{i=1}^3 U_{li}^* |\nu_i\rangle \quad (1.4)$$

where U_{li}^* denotes the Pontecorvo-Maki-Nakagawa-Sakata (PMNS) matrix, named after the Physicists that proposed the model [9].

$$U = \begin{pmatrix} c_{12}c_{13} & s_{12}c_{13} & s_{13}e^{-i\delta} \\ -s_{12}c_{23} - c_{12}s_{23}s_{13}e^{i\delta} & c_{12}c_{23} - s_{12}s_{23}s_{13}e^{i\delta} & s_{23}c_{13} \\ s_{12}s_{23} - c_{12}c_{23}s_{13}e^{i\delta} & -c_{12}s_{23} - s_{12}c_{23}s_{13}e^{i\delta} & c_{23}c_{13} \end{pmatrix} \cdot \begin{pmatrix} 1 & 0 & 0 \\ 0 & e^{i\alpha} & 0 \\ 0 & 0 & e^{i\beta} \end{pmatrix} \quad (1.5)$$

where $c_{ij} = \cos \theta_{ij}$ and $s_{ij} = \sin \theta_{ij}$ with the mixing angles $\theta_{ij} \in [0, \frac{\pi}{2})$. The Dirac phase δ is responsible for CP violation, while the two phases α and β , which also cause CP violation, only exist if the neutrino is a Majorana particle (more on the neutrino nature in section 1.3). The probability for a flavor change can then be expressed as

$$P(\nu_\alpha \rightarrow \nu_\beta) = \delta_{\alpha\beta} - 4 \sum_{j>i} \text{Re} \left(J_{\alpha\beta}^{ij} \right) \sin^2 \left(\frac{\Delta_{ij}}{2} \right) + 2 \sum_{j>i} \text{Im} \left(J_{\alpha\beta}^{ij} \right) \sin(\Delta_{ij}) \quad (1.6)$$

$$\text{with } ij_{\alpha\beta} = U_{\beta i} U_{\alpha i}^* U_{\beta j}^* U_{\alpha j} \quad \text{and} \quad \frac{1}{2} \Delta_{ij} \approx 1.27 \left(\frac{\Delta m_{ij}^2}{\text{eV}^2} \right) \left(\frac{L}{\text{km}} \right) \left(\frac{\text{GeV}}{E} \right)$$

The transition probability depends therefore on the energy E , the distance traveled L , the Elements of the PMNS matrix and the mass-squared difference $\Delta m_{ij}^2 = m_j^2 - m_i^2$ of mass eigenstates i and j . For neutrino oscillations to occur Δm_{ij}^2 can't be 0 and therefore at least two mass eigenstates need to be massive.

Analysing neutrinos oscillations these mass differences can be estimated. With atmospheric neutrinos $|\Delta_{31} m^2| \approx |\Delta_{32} m^2| \equiv \Delta m_{\text{atm}}^2$ was measured, while solar neutrinos were used for $\Delta_{21} m^2 \equiv \Delta m_{\text{sol}}^2$. Additionally the sign of Δm_{sol}^2 can be determined using

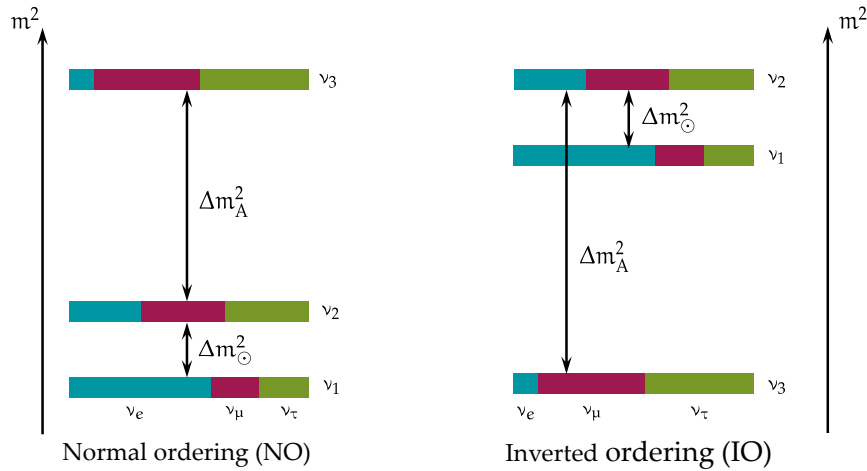


Figure 1.1: The two different possibilities for neutrino mass ordering. For the normal ordering ν_1 is the lightest mass eigenstate, while in case of inverted ordering ν_3 is the lightest. The mass eigenstates are a superposition of their flavor eigenstates. Picture from [11]

the Mikheyev-Smirnov-Wolfenstein (MSW) effect, which modifies solar neutrino oscillations within matter by a matter resonance effect [10]. The sign for Δm_{atm}^2 is unknown because experiments are not sensitive to it yet.

This leads to two different scenarios shown in Figure 1.1:

- Normal ordering where ν_1 is the lightest mass eigenstate
- Inverted ordering where ν_3 is the lightest

Which of those two possible scenarios describes our reality is currently under investigation by several different experiments.

1.3 Double Beta Decay

Next to their mass, one of the biggest mysteries surrounding neutrinos is their intrinsic nature. As hinted in formula 1.5 of Section 1.2.2 there are two possible scenarios for the neutrino. Either they are

- Dirac fermions \rightarrow neutrinos and antineutrinos are different particles;
- Majorana fermions \rightarrow neutrinos are their own antiparticles.

The most practical way to test the hypothesis of the majorana nature experimentally is the neutrinoless double beta Decay. This process is an alternative version of the two

neutrino double beta decay ($2\nu\beta\beta$ -decay), only possible if the neutrino is a majorana particle.

The mechanism of $2\nu\beta\beta$ -decay is explained the binding energy for atomic nuclei, which is described by the Bethe-Weizäcker mass formula:

$$m(A, Z) = \alpha \cdot A - \beta \cdot Z + \gamma \cdot Z^2 + \frac{\delta}{\sqrt{A}} \quad (1.7)$$

with δ the pairing energy, here for example for a core with $A = 76$:

$$\delta = \begin{cases} -11.2 \text{ MeV}/c^2 & \text{if } Z \text{ and } N = A - Z \text{ are even} \\ 0 & \text{if } A \text{ is odd} \\ +11.2 \text{ MeV}/c^2 & \text{if } Z \text{ and } N = A - Z \text{ are odd} \end{cases} \quad (1.8)$$

The resulting mass parabolas for a nucleus with $A = 76$ are shown in figure 1.2. Normally atomic cores with neutron/proton excess decay via β^-/β^+ decays to their energetically most optimal state. But there exist some isotopes, for example ^{76}Ge , where the β decay into ^{76}As is not possible, but undergoing two subsequent β decays into ^{76}Se would lead to an energetically more stable state.

For isotopes like ^{76}Ge a new decay mode was first predicted by Goeppert-Mayer in 1935 [12], the $2\nu\beta\beta$ decay:

$$(A, Z) \rightarrow (A, Z + 2) + 2e^- + 2\bar{\nu}_e \quad (1.9)$$

This interaction is a second order weak process. Therefore it contains two weak interaction vertices and the channel is strongly suppressed. That means that for the isotopes where the interaction has been experimentally observed, the decay has quite high half-live of $T_{1/2}^{2\nu} > 10^{18}$ yr [13].

If the neutrino were a majorana particle, the $0\nu\beta\beta$ decay would be possible as an alternative decay channel. It was first suggest in 1938 by W.H.Furry [14] and would violate lepton number conservation. $0\nu\beta\beta$ decay predicts that the core decays without emitting two electron anti neutrinos:

$$(A, Z) \rightarrow (A, Z + 2) + 2e^- \quad (1.10)$$

In the standard interpretation, $0\nu\beta\beta$ decay is mediated by light massive Majorana neutrinos. The Feynmann diagram for the interaction can be seen in 1.3.

While the realization of $0\nu\beta\beta$ decay could be made by the neutrino exchange, several other extensions of the Standard Model are also possible. The Schechter-Valle Theorem

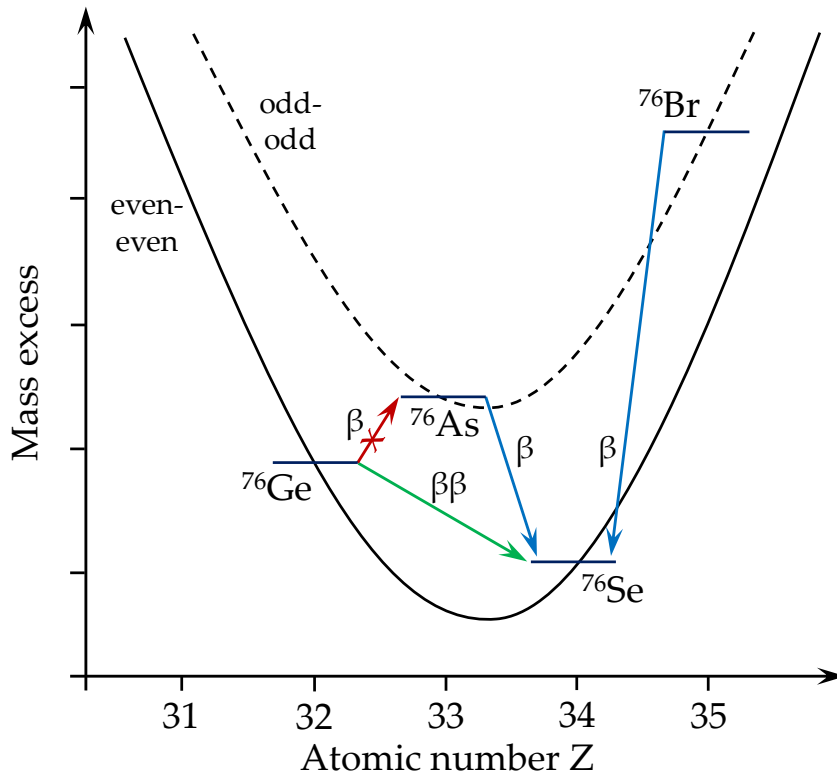
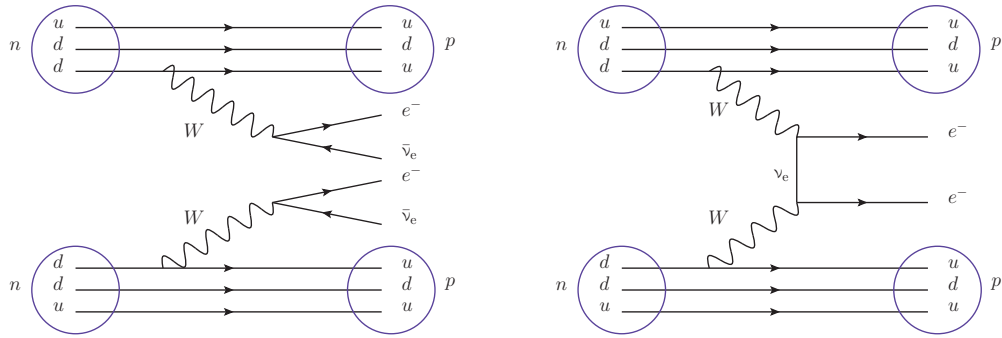


Figure 1.2: Mass parabolas for even-even and odd-odd nuclei using the example of isobars with mass number $A = 76$. Isobars with even mass and atomic number lie on a lower parabola (straight line) compared to those with odd atomic number (dotted line). Typically, transitions between the curves are realized via single beta decay. In some cases, however, the neighboring isobar is energetically higher and single beta decay is forbidden, e.g. ${}^{76}\text{Ge} \not\rightarrow {}^{76}\text{As}$. Then, two-neutrino double beta decay is the only allowed decay mode. Picture and caption from [11]

states that for all of these extensions, $0\nu\beta\beta$ decay includes a non-zero effective Majorana mass term, indicating the Majorana nature of neutrinos [15].

$0\nu\beta\beta$ decay has not yet been observed. Its signature is detectable in the energy spectrum of the electrons released by the decay. In the case of $2\nu\beta\beta$ decay, the energy released in the process, $Q_{\beta\beta}$, is shared between the electrons and the neutrinos, resulting in a continuous distribution between 0 and $Q_{\beta\beta}$ in the energy spectrum of the 2 electrons. In contrast, for $0\nu\beta\beta$ decay, the entire energy is carried by the two electrons, which would create a distinct peak in the energy spectrum. This is illustrated in 1.4.

If the $0\nu\beta\beta$ decay is mediated via light neutrinos, the half life can be estimated according to Fermi's golden rule with:



(a) Two-neutrino double beta decay ($2\nu\beta\beta$ decay). (b) Neutrinoless double beta decay ($0\nu\beta\beta$ decay)

Figure 1.3: Feynman diagrams of (a) $2\nu\beta\beta$ decay and (b) $0\nu\beta\beta$ decay assuming light neutrino exchange. Figure from [11]

$$\Gamma_{0\nu} = \frac{1}{T_{0\nu}^{1/2}} = G_{0\nu}(Q_{\beta\beta}, Z) |\mathcal{M}_{0\nu}|^2 \left(\frac{m_{\beta\beta}}{m_e} \right)^2 \quad (1.11)$$

Here, $G_{0\nu}(Q_{\beta\beta}, Z)$ denotes the phase space factor, which is proportional to Z and $Q_{\beta\beta}^5$, the Nuclear Matrix Element, which can be calculated from nuclear theory, and $\langle m_{\beta\beta} \rangle$, the effective Majorana mass, which is the mass observable for the process.

$\langle m_{\beta\beta} \rangle$ is the coherent sum of the different neutrino mass eigenstates m_i weighted with the PMNS mixing matrix elements U_{ij} :

$$m_{\beta\beta} = \left| \sum_{i=1}^3 U_{ei}^2 m_i \right| = \left| (c_{12}^2 c_{13}^2 e^{2i\alpha}) m_1 + (s_{12}^2 c_{13}^2 e^{2i\beta}) m_2 + (s_{13}^2 e^{-2i\delta}) m_3 \right| \quad (1.12)$$

Depending of the exact values for the masses of the neutrino mass eigenstates m_i and the phases α and β , three different regimes could be observed for $\langle m_{\beta\beta} \rangle$, as illustrated in Figure 1.5.

- Inverted mass ordering (IO), in which m_3 is the lightest neutrino mass eigenstate. This scenario would lead to a flat band for $\langle m_{\beta\beta} \rangle$.
- Normal mass ordering (NO), where m_1 is the lightest neutrino mass eigenstate. In this case, in addition to the flat band in the region $m_{\text{lightest}} < 10^{-3}$ eV, there is a possibility that $\langle m_{\beta\beta} \rangle$ vanishes for 10^{-2} eV $>$ $m_{\text{lightest}} >$ 10^{-3} eV.
- Quasi-degenerate regime, where IO and NO can't be distinguished from each other.

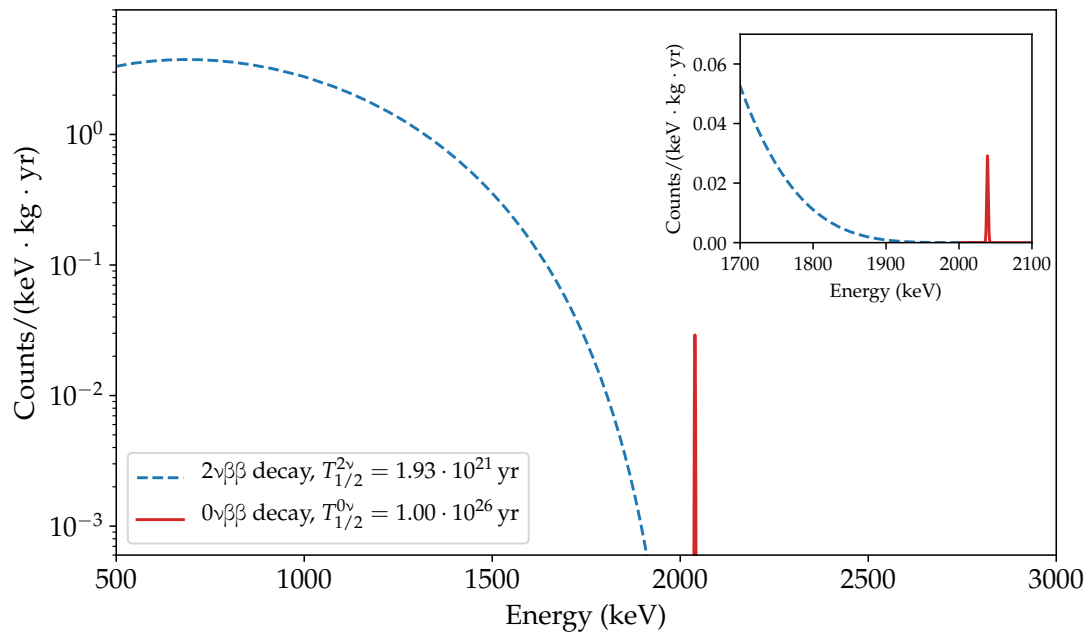


Figure 1.4: Energy spectrum depicting the experimental signatures of $2\nu\beta\beta$ and $0\nu\beta\beta$ decay for ^{76}Ge with $Q_{\beta\beta} \approx 2039$ keV. The $2\nu\beta\beta$ decay shows a continuous spectrum, whereas $0\nu\beta\beta$ exhibits a sharp peak at the $Q_{\beta\beta}$ -value, with its width determined by energy resolution. Figure from [11], based on data by Y. Kermaïdic.

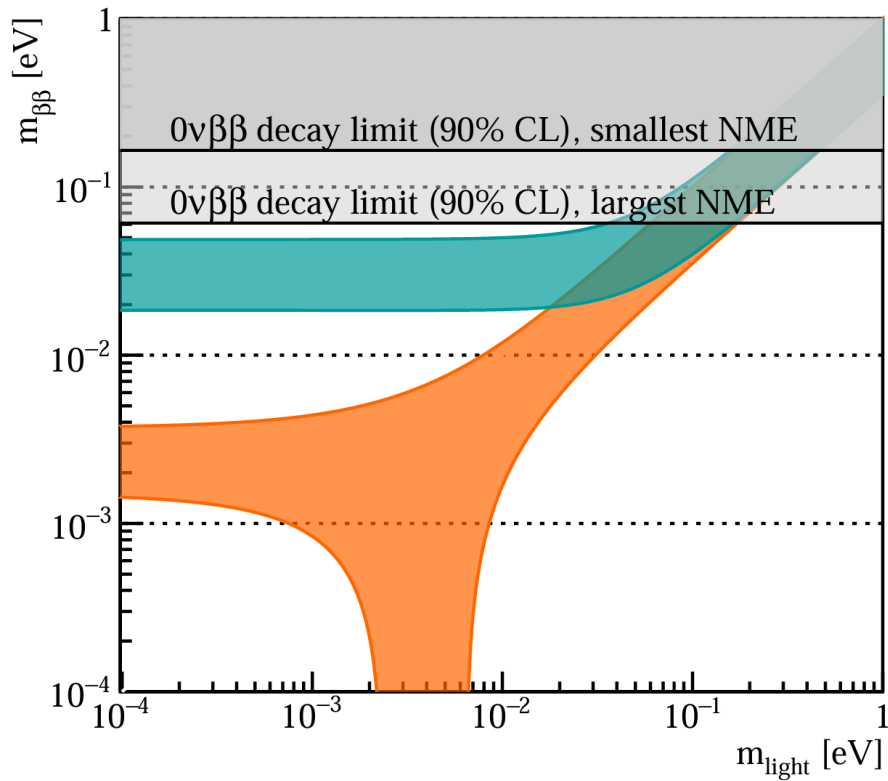


Figure 1.5: The effective Majorana mass $\langle m_{\beta\beta} \rangle$ is shown as a function of the lightest neutrino mass m_{lightest} . The bands represent normal mass ordering (orange) and inverted mass ordering (green), with widths corresponding to the best-fit values of neutrino oscillations parameters from [16] and Majorana phases α and β varying from $[0, 2\pi]$. The grey areas correspond to region currently excluded by the best $0\nu\beta\beta$ decay experiments [17]. Figure from [18].

Chapter 2

Semiconductor Detectors

Numerous experiments aim to detect $0\nu\beta\beta$ using a variety of technologies, each with its own set of benefits and challenges. One promising approach is the use of semiconductor detectors, which will be discussed in detail in this chapter.

2.1 Properties of semiconductors

Electrons in solids can be described by a model where they occupy energy bands. The most significant of these are the valence band, which is fully occupied with electrons at absolute zero ($T=0$ K), and the conduction band, located just above the valence band. Electrons in the conduction band can move freely, thereby contributing to electrical conductivity. In conductors, the valence and conduction bands overlap, allowing easy electron movement between the bands. In insulators, a large energy gap (greater than 5 eV) separates these bands, leaving the conduction band empty and preventing electrical conductivity. Semiconductors have a smaller energy gap, which allows some valence electrons to gain sufficient thermal energy to move from the valence band to the conduction band. This probability of an electron overcoming the band gap by thermal excitation is described by the Boltzmann distribution [19].

$$P(T) \propto T^{3/2} \exp\left(-\frac{E_g}{2kT}\right) \quad (2.1)$$

Here, T is the temperature, k the Boltzmann constant, and E_g the band gap energy. When an electron jumps to the conduction band it leaves behind a hole in the valence band. This pair of excited electron and hole is called electron-hole pairs. This is illustrated in 2.2.

Electrons can reach the conduction band not only through thermal excitation but also by transitioning when a charged particle or photon strikes the semiconductor. This

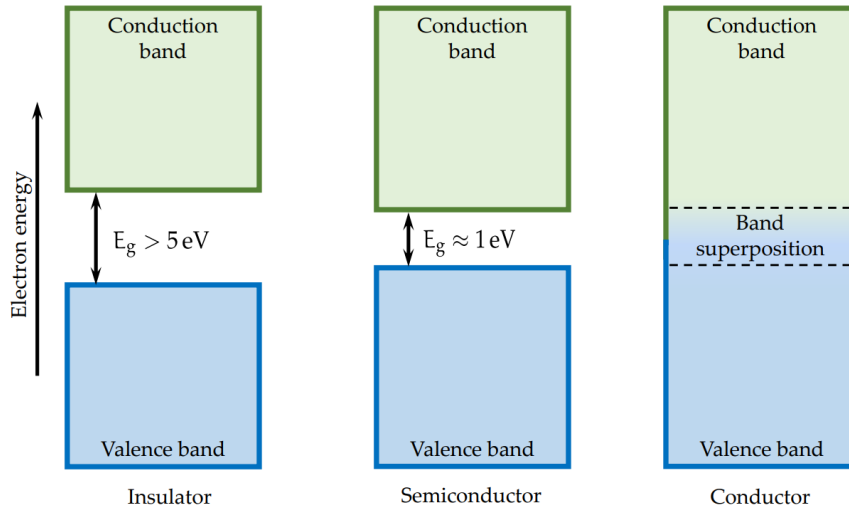


Figure 2.1: The band structure for different types of materials. Insulators have large band gaps, while Semiconductors have smaller ones. Conductors don't have a gap between valence and conduction band. Figure from [11]

interaction creates electron-hole pairs in direct proportion to the absorbed energy E_{abs} :

$$n = \frac{E_{abs}}{\epsilon(T)} \quad (2.2)$$

Here $\epsilon(T)$ is the average energy needed to create an electron-hole pair. Represents the average energy required to create an electron-hole pair. This energy is temperature-dependent and varies for different materials. For example, in the case of Germanium, $\epsilon(T)$ is [20]:

$$\epsilon(T) = 2.2 \cdot E_g(T) + 1.99 \cdot E_g^{3/2}(T) \cdot \exp\left(\frac{4.75E_g(T)}{T}\right) \quad (2.3)$$

Where, the temperature-dependent band gap E_g for Germanium can be described by Varshni's empirical relation [21, 22]:

$$E_g(T) = E_g(0\text{K}) - \frac{4.774 \times 10^{-4} \text{ eV K}^{-2} \cdot T^2}{T + 235 \text{ K}} \quad (2.4)$$

Figure 2.3 shows how the average citation energy $\epsilon(T)$ and the band gap transition probability $P(T)$ change for different temperatures.

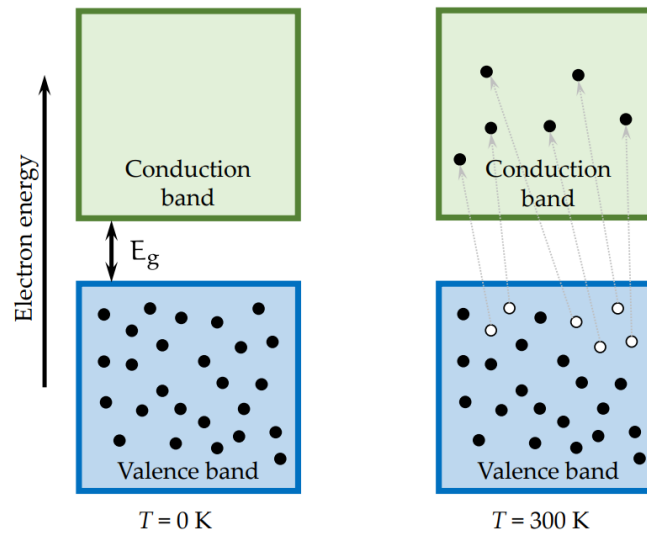


Figure 2.2: The band structure for different types of materials. Insulators have large band gaps, while Semiconductors have smaller ones. Conductors don't have a gap between valence and conduction band [11].

2.2 Detector working principle

The mechanism of energy deposition in a material leading to the creation of electron-hole pairs can be utilized to build semiconductor detectors. By collecting these electron-hole pairs, the energy deposited by a particle hitting the detector can be calculated using the linear proportion described in equation 2.2. To vary the number of electron-hole pairs generated by the same energy, the temperature can be adjusted to modify the temperature-dependent $\epsilon(T)$. To maximize the number of electron-hole pairs, which is usually desired to increase signal strength, the temperature should be increased because $\epsilon(T)$ becomes smaller at higher temperatures, as illustrated in 2.3a. However, the probability of thermal excitations $P(T)$ creating electron-hole pairs also increases with temperature, as shown in formula 2.1 and visualized in 2.3b. When these electron-hole pairs are read out, they produce a noise signal known as leakage current, which degrades the signal quality and should ideally be minimized. Therefore, for practical applications, a compromise must be found for the temperature to make $\epsilon(T)$ small while not allowing $P(T)$ to become too large. Typically, cryogenic temperatures of Liquid Nitrogen ($T = 77 \text{ K}$) or Liquid Argon ($T = 87 \text{ K}$) are used for Germanium detectors.

A semiconductor usually can't be fabricated to be purely out of one material. There are always some impurities in the crystal, which can affect the band gap of the semiconductor. Silicon or Germanium are elements with 4 valence electrons. If elements with only 3 valence electrons are present in the lattice, this adds a hole into the lattice, depicted

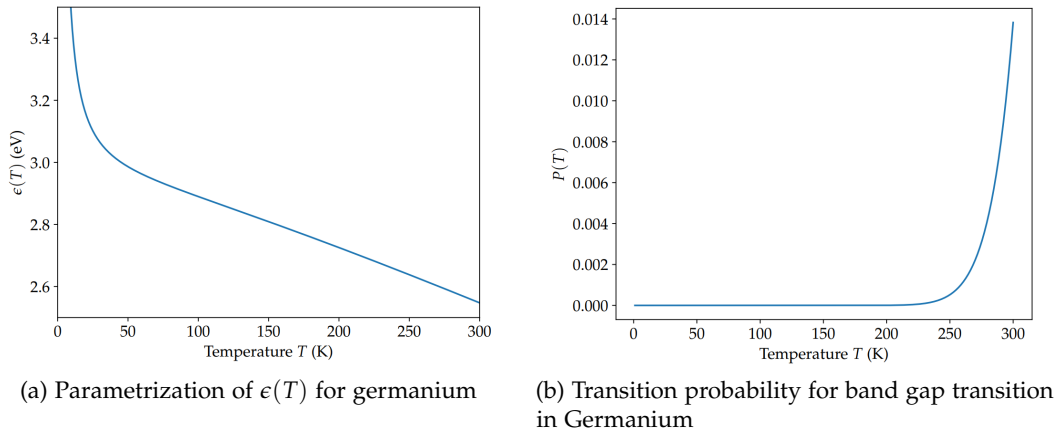


Figure 2.3: Parametrizations of $\epsilon(T)$ and the transition probability $P(T)$ for germanium as functions of temperature. Figures from [11].

in 2.4a. Materials with this kind of impurity are called p-type (presence of positive acceptor impurities). Conversely, if an atom with 5 valence electrons is added to the crystal lattice, the impurity atom donates an extra electron to the material, creating n-type material (presence of negative donor impurities), as seen in 2.4b. Usually, a crystal has both types of impurities, but these impurities can also be deliberately added in a process called doping to create n-type and p-type material, for example, to make contacts for the readout electronics of the detector [19].

When n-type and p-type materials are placed next to each other, they form a diode. At the junction, known as the p-n junction, electrons drift from the n-type material to fill holes in the p-type material. This creates a region called the depletion zone, where no free charge carriers remain. This region, depicted in 2.5, is used as the active volume of the semiconductor detector. Typically, this region is not very large, but it can be extended by applying a high voltage in the so called reverse bias direction, where a negative potential is applied to the p-side with respect to the n-side of the junction. The relationship between the depletion region depth and applied voltage V_{bias} can be described by [19]:

$$d \propto \left(\frac{V_{bias}}{e \cdot N_{impurity}} \right)^{1/2} \quad (2.5)$$

Where $N_{impurity}$ is the concentration of impurities. When the voltage is flipped, the junction is configured in forward bias. Here the voltage decreases the size of the depletion region, even allowing current to flow through the junction if the voltage is high enough.

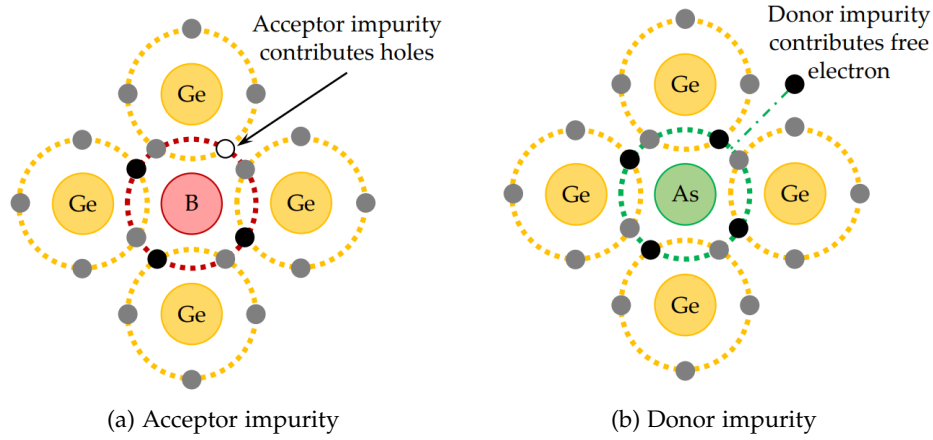


Figure 2.4: Acceptor and donor impurities in germanium, a group IV element. In 2.14a, boron acts as an acceptor impurity from group III, creating an additional hole (p-type). Arsenic, a group V element, serves as a donor impurity, introducing an extra electron (n-type). Figures from [11].

2.3 Germanium detectors in LEGEND

Typically germanium detectors are constructed from a single crystal of p-type material. The p^+ contact, functioning as the signal readout, is created by boron implantation to form a p-type junction with a thickness of approximately 100 nm. The n^+ contact, is created by diffusing lithium onto the detector's surface to reach a thickness of about 1-2 mm. To obtain an active region on the order of centimeters, the impurity concentration must be around 10^{10} atoms cm^{-3} with a reverse bias voltage on the order of kilovolts. Germanium detectors that contain such low levels of impurity are referred to as high purity germanium (HPGe) detectors. These are crucial to realise $0\nu\beta\beta$ searches, where big active volumes are beneficial.

2.3.1 Signal formation and weighting potential

When a positive high voltage (HV) is applied to the n^+ contact, the detector bulk becomes fully depleted. When a particle enters the bulk of the detector, it generates electron-hole pairs when interacting with the detector material. This initiates the signal formation process: as the electrons and holes drift towards their respective electrodes, they induce mirror charges until the last electron-hole pairs are collected at the electrodes. The duration for the complete collection of these charges is known as the drift time, τ_{drift} . The net observable charge $Q(t)$ and the current $I(t)$ at the electrodes can be determined using the Shockley-Ramo theorem [23, 24]:

$$Q(t) = -Q \cdot [\Phi(\vec{r}_h(t)) - \Phi(\vec{r}_e(t))] \quad (2.6)$$

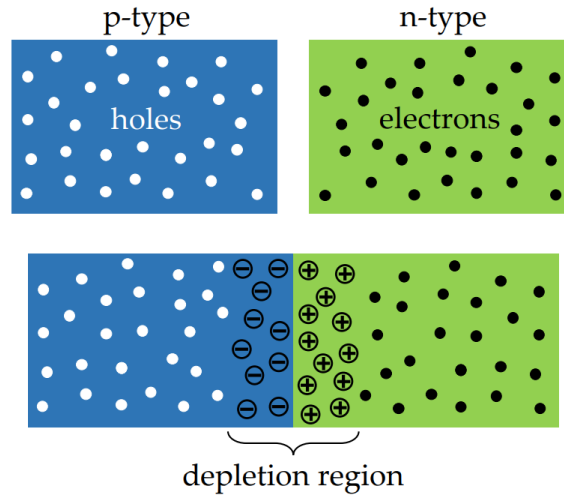


Figure 2.5: Schematic of a combination of p-type and n-type detector materials. Free electrons and holes diffuse into the opposite material, where they recombine, leaving a depletion zone without any free charge carriers. Figure from [11].

$$I(t) = Q \cdot \left[\vec{E}(\vec{r}_h(t)) \cdot \vec{v}_h(t) - \vec{E}(\vec{r}_e(t)) \cdot \vec{v}_e(t) \right] \quad (2.7)$$

Here, Q represents the total charge of the incoming particle, $\Phi(\vec{r})$ is the weighting potential, and $\vec{E}(\vec{r})$ is the weighting field at position \vec{r} . The position and velocity of the hole (electron) cloud at time t are denoted by $\vec{r}_{h(e)}(t)$ and $\vec{v}_{h(e)}(t)$, respectively. The weighting potential $\Phi(\vec{r})$ that can be computed by solving the Laplace equation

$$\nabla^2 W_p = 0 \quad (2.8)$$

for a specific detector geometry with the boundary conditions that the voltage at the p^+ contact is unity, $\Phi(\vec{r}_{p^+}) = 1$, and zero at the n^+ contact, $\Phi(\vec{r}_{n^+}) = 0$, which is often solved numerically. The weighting field describing the coupling strength of the charge to the electrode at a given detector position can then be obtained by the gradient of the weighting potential [19]:

$$\vec{E}(\vec{r}) = \nabla \Phi(\vec{r}) \quad (2.9)$$

2.3.2 Detector geometries

Over the years, the scientific community exploring $0\nu\beta\beta$ decay in ^{76}Ge has utilized several different germanium detector geometries. The various detector types are depicted in Figure 2.16, alongside their simulated weighting potential and the paths that events in the bulk would follow during drift.

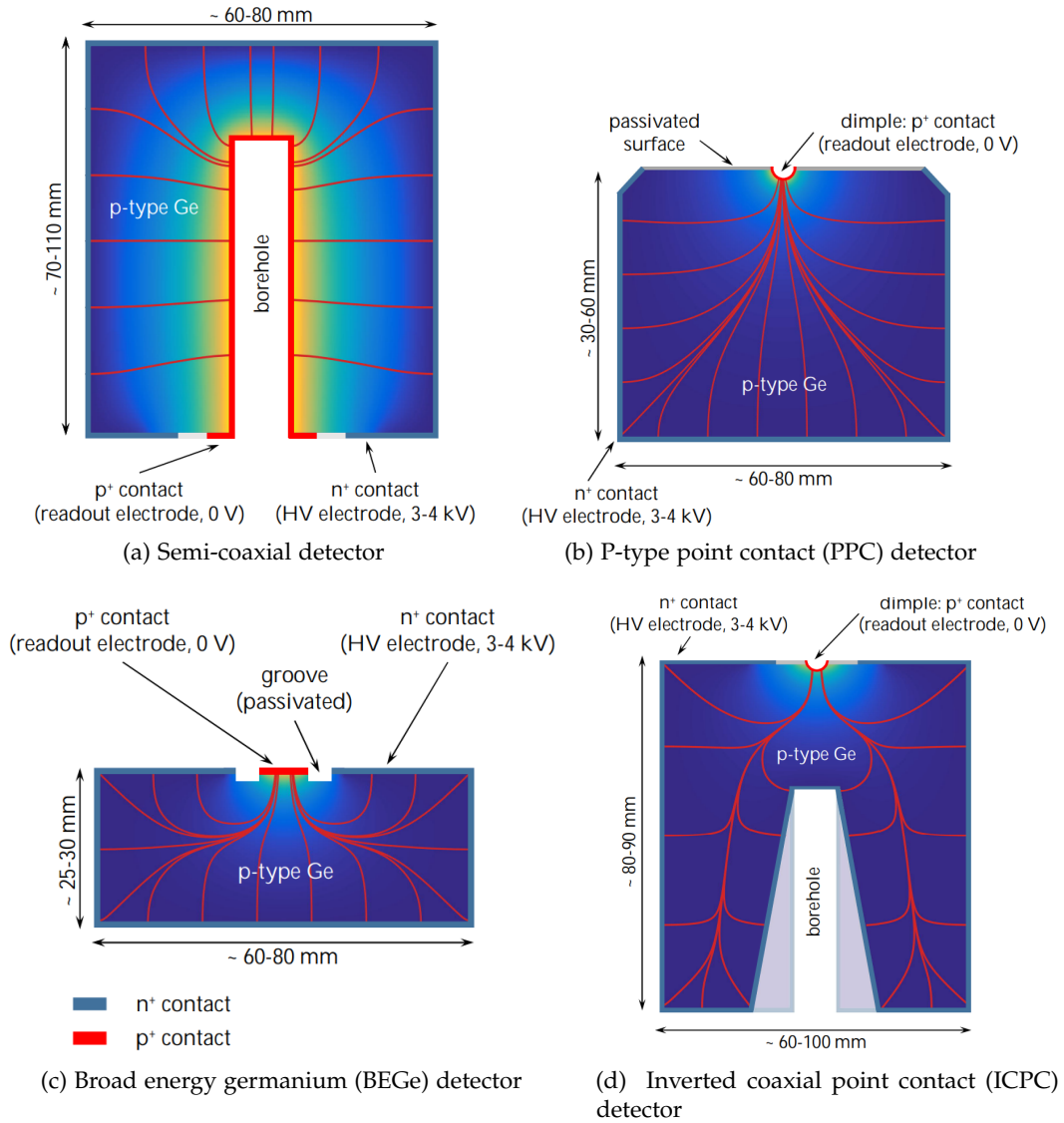


Figure 2.6: Sketches of the different detector types typically used in ^{76}Ge -based $0\nu\beta\beta$ decay searches: (a) Semi-coaxial, (b) PPC, (c) BEGe, and (d) ICPC detector. The figure shows the electrode arrangements and indicates typical dimensions. Moreover, the weighting potential inside the detector (blue and yellow areas correspond to low and high values, respectively), and the drift paths (red thin lines) are illustrated. Figure and caption from [11].

- **Semi-coaxial detectors:** Initially deployed in ^{76}Ge -based experiments [25, 26], these detectors feature a cylindrical shape with a bore hole and a large p+ electrode covering it. They suffer from higher capacitance ($C_D \approx \text{O}(10 \text{ pF})$), resulting in poorer energy resolution. Due to the shape of weighting potential they also suffer from limited background rejection effectiveness.
- **P-type point contact (PPC) detectors:** Developed as an improvement over semi-coaxial designs, PPC detectors have a smaller cylindrical shape with a central point contact on the top surface. This design reduces capacitance ($C_D \approx 1\text{--}2 \text{ pF}$), enhancing energy resolution and enabling operation at lower thresholds ($< 1 \text{ keV}$) [27]. Their geometry supports effective background rejection based on signal shape, making them suitable for efficient $0\nu\beta\beta$ decay searches [28].
- **Broad energy germanium (BEGe) detectors:** Similar to PPC detectors, BEGe detectors have low capacitance ($C_D \approx 3\text{--}5 \text{ pF}$), but in contrast feature a larger signal readout electrode (up to 7 mm radius) which is separated from the n+ contact by a groove. This makes the detector less sensitive to surface backgrounds, enhancing performance in low-background environments [29].
- **Inverted coaxial point contact (ICPC) detectors:** Designed to increase detector mass in $0\nu\beta\beta$ decay searches, ICPC detectors feature a cylindrical shape with a longer length compared to PPC and BEGe detectors. They maintain low capacitance and excellent background rejection capabilities, allowing for larger detector masses (up to 4 kg). However, their extended size alters timing characteristics, requiring careful management of charge cloud effects during signal detection [30].

2.4 Interaction of particles with matter

A thorough understanding of particle interactions with matter is crucial for comprehending radiation detection with semiconductor detectors. Depending on the properties of the incoming particle and the characteristics of the absorber material, various interaction processes can occur.

2.4.1 Charged particles

Heavy charged particles (masses $> 1 \text{ GeV}$) interact electromagnetically with the shell electrons of atoms and lose energy through inelastic collisions, leading to ionized atoms [19]. For the interaction of a single charge particle the ionization energy loss dE/dx per unit path length dx is described by the Bethe-Bloch Formula [19]:

$$-\left\langle \frac{dE}{dx} \right\rangle = \frac{4\pi e^4 z^2}{m_e v^2} N Z \left[\log \left(\frac{2m_e v^2}{I} \right) - \log(1 - \beta^2) - \beta^2 \right] \quad (2.10)$$

Here, ze describes the charge of the incoming particle in multiples of the electron

charge, m_e is the electron rest mass, $v = \beta c$ the velocity, N the number density, Z the atomic number, and I is the average excitation and ionization potential of the absorber material. The formula assumes that the mass of the incoming particle is much higher than the electron mass, resulting in minimal deflection of the incoming particle and a small energy transfer per interaction to the materials electrons compared to the particle's kinetic energy. The term NZ represents the electron density of the absorber material, indicating that materials with higher densities exhibit greater stopping power. Alpha particles have an charge of $z = 2$, which means they ionize strongly due to the z^2 -dependence in Eq. (2.10), resulting in a short mean free path and interactions basically occurring at a single site [19].

Since the Bethe formula in Equation 2.10 assumes that the mass of the incoming particle is much larger than that of the shell electrons, a condition not applicable to electrons and positrons. This changes their energy loss mechanisms and adds complexity to it: low energy electrons suffer their energy loss primarily through ionization, while above a critical energy E_c , Bremsstrahlung, the emission of photons in the electrostatic field of a nucleus, becomes the main contributor. The approximation for the critical energy E_c is given by [31]:

$$E_c \approx \frac{800 \text{ MeV}}{Z}, \quad E_{\text{Ge}}^c \approx 25 \text{ MeV}. \quad (3.2)$$

Positrons experience a similar energy loss like electrons. They only differentiate when the positron is at rest ($E_{e^+} \lesssim 10 \text{ keV}$), at which point it forms positronium before it consequently annihilate with an electron from the surrounding material, producing two photons, each with an energy of $E_\gamma = 511 \text{ keV}$ [19].

2.4.2 Gamma radiation

The interactions of the highly penetrating Gamma radiation are significantly influenced by both the energy of the radiation and the atomic number of the absorber material. The attenuation of gamma rays in terms of mass attenuation follows the Beer-Lambert law[19], which describes the radiation intensity $I(x)$ as:

$$I(x) = I_0 e^{-\left(\frac{\mu}{\rho}\right)\lambda}, \quad \lambda = \rho x \quad (2.11)$$

where I_0 is the initial intensity, μ is the linear attenuation coefficient, and ρ is the mass density of the absorber material. The mass attenuation coefficient $\frac{\mu}{\rho}$ can then be divided into the cross section sum of the different processes σ_i :

$$\frac{\mu}{\rho} \propto \sum_i \sigma_i \propto \sigma_{PA} + \sigma_{IS} + \sigma_{PP}, \quad (2.12)$$

Figure 2.7 shows the radiation intensity $I(x)$ for different energies as well as the contributions of the three different main interaction modes:

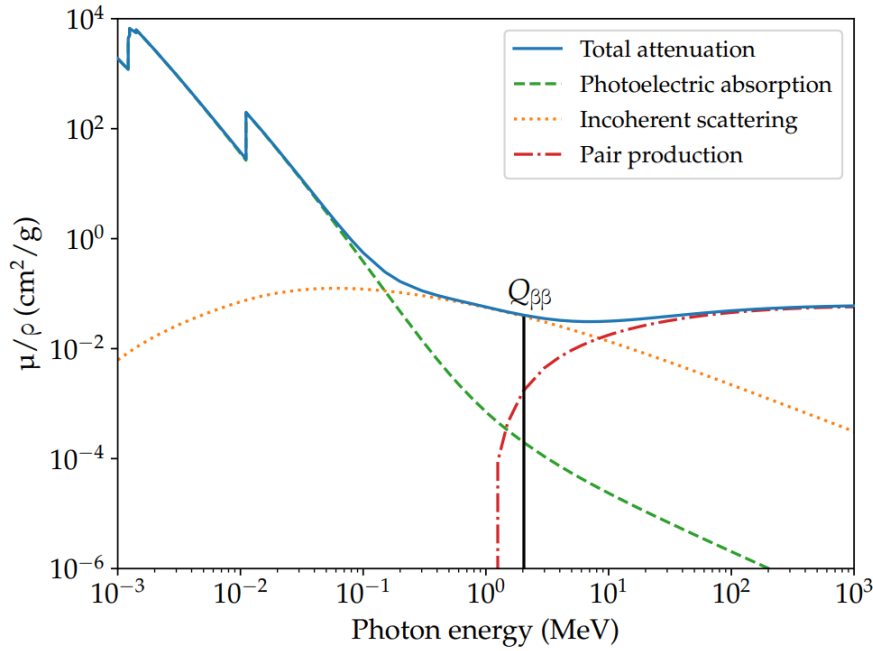


Figure 2.7: Attenuation coefficient μ/ρ in ^{76}Ge as a function of photon energy E_γ , illustrating the main processes: photoelectric absorption (PA), incoherent scattering (IS), and pair production (PP) in their respective energy ranges. Figure from [11].

- **Photoelectric Absorption (PA):** This process dominates at low energies up to approximately 150 keV for ^{76}Ge . The incident photon is entirely absorbed by a shell electron, which is then emitted, leaving the absorber atom in an excited state. This state de-excites by emitting characteristic X-ray photons or Auger electrons. If the energy of the incident electron is fully deposited in the active volume of the detector, a characteristic peak called the full energy peak (FEP) appears in the energy spectrum [19].
- **Incoherent Scattering (IS) (Compton Scattering):** In the intermediate energy range from 150 keV to 8 MeV, this process is most dominant for ^{76}Ge . A photon scatters off a bound or free electron at an angle $0 \leq \theta \leq \pi$ relative to its initial direction, with the scattered photon's energy given by:

$$E'_\gamma = \frac{E_\gamma}{1 + \frac{E_\gamma}{m_e c^2} (1 - \cos \theta)}$$

The difference in energy is transferred to the recoiling electron. This process creates the Compton continuum in the energy spectrum, with the Compton edge

as a noticeable shoulder at the maximum electron energy:

$$\max(E_e) = E_e(\theta = \pi) = \frac{2E_\gamma^2}{2E_\gamma + m_e c^2}$$

as shown in Figure 2.8.

- **Pair Production (PP) and Pair Annihilation:** Dominant at high energies above 8 MeV for ^{76}Ge . If the initial γ energy exceed two times the rest mass of an electron (1022 keV), an incident photon can interact with a nucleus to produce an electron-positron pair:

$$E_{\text{pair}} = E_\gamma - 2m_e c^2 \quad \text{with} \quad E_\gamma \geq 2 \times 511 \text{ keV}$$

The positron then slows down in the absorber material and annihilates with an electron, emitting two 511 keV photons in opposite directions. This leads to 4 characteristic peaks in a germanium detector, depending on where the initial process happened:

- **Outside Detector:** One of the two photons enters the active volume, producing a 511 keV peak in the energy spectrum.
- **Inside Detector:**
 - * Both photons are absorbed, resulting in a full energy peak (FEP) at the full initial photon energy E_γ .
 - * One photon escapes, creating a single escape peak (SEP) at $E_\gamma - 511 \text{ keV}$.
 - * Both photons escape, forming a double escape peak (DEP) at $E_\gamma - 2 \times 511 \text{ keV}$.

The spectral features of the Compton edge and the different peaks created by Pair production and annihilation are depicted in Figure 2.8 for a ^{228}Th calibration measurement using a germanium detector.

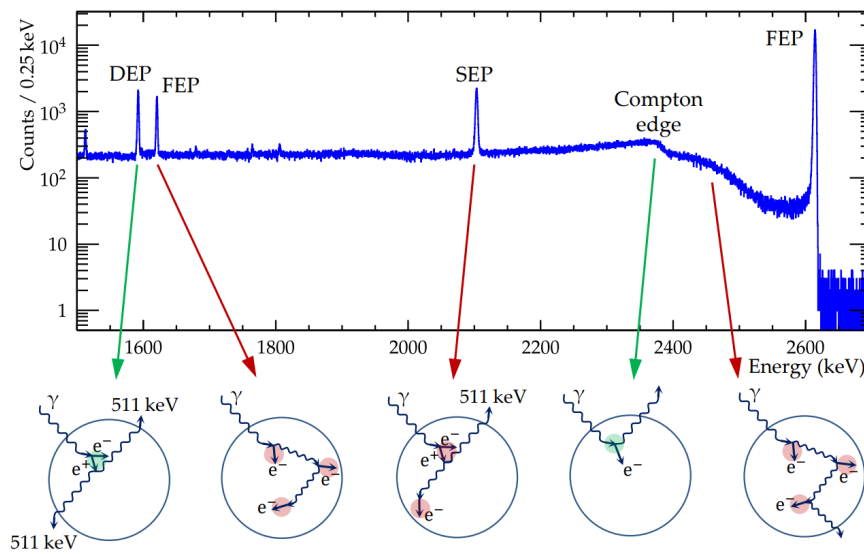


Figure 2.8: Energy spectrum of a ^{228}Th calibration measurement: The full energy peak (FEP) represents events where the entire energy of the incident photon is absorbed in the active volume. The single escape peak (SEP) occurs when one of the annihilation photons escapes the active volume, and the double escape peak (DEP) appears when both annihilation photons escape. The Compton edge is characterized by the maximum deflection angle of the incident photon during Compton scattering, with events beyond the Compton edge resulting from multiple Compton scattering. Figure from [11].

Chapter 3

The LEGEND Experiment

The Large Enriched Germanium Experiment for Neutrinoless Double Beta Decay (LEGEND) is one of the most promising experiments searching for $0\nu\beta\beta$ decay. In this chapter, the techniques used by the collaboration to set the leading limit for $0\nu\beta\beta$ decay in ^{76}Ge will be discussed.

3.1 Overview

The LEGEND experiment builds upon the GERDA (GERmanium Detector Array) [32] and MAJORANA experiments [33], both of which utilized high-purity germanium detectors enriched in ^{76}Ge . GERDA, conducted at Gran Sasso National Laboratory, achieved significant background suppression by developing the LAr-veto system and set the best limits so far on the $0\nu\beta\beta$ in ^{76}Ge half-life of $T_{1/2}^{0\nu} > 1.8 \times 10^{26}$ yr (90% CL) [32]. MAJORANA, at the Sanford Underground Research Facility, reached the best energy resolution for $0\nu\beta\beta$ search in ^{76}Ge with clean material and read out electronics very close to the detector [28]. By combining techniques from GERDA and MAJORANA, the LEGEND collaboration seeks to achieve unprecedented sensitivity in the search for $0\nu\beta\beta$ in ^{76}Ge and improve on the results accomplished by its predecessors. This is illustrated in 3.1.

Germanium detectors offer several advantages in the search for $0\nu\beta\beta$ in ^{76}Ge :

- **Superior Energy Resolution:** Germanium detectors provide excellent energy resolution in order of 0.1% FWHM [33], crucial for distinguishing the potential $0\nu\beta\beta$ decay in ^{76}Ge signal from background events.
- **Low Background Levels:** Achieving ultra-low background levels is a significant strength, enabled by advances in detector material purity and shielding techniques.

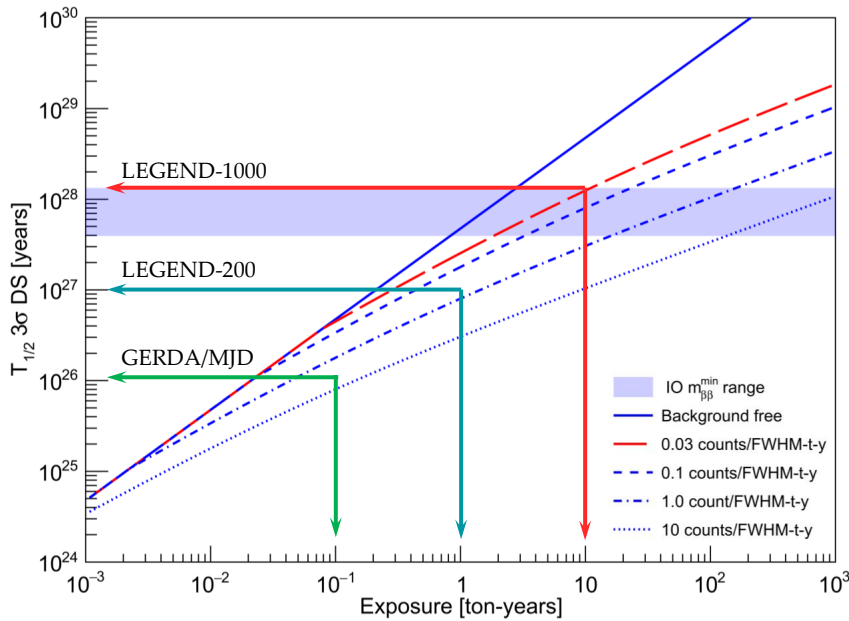


Figure 3.1: Experimental sensitivity in terms of half-life $T_{1/2}^{0\nu}$ as a function of exposure $M \cdot t$ for ^{76}Ge . While the blue band shows the allowed region for the inverted ordering (IO), the solid blue line symbolizes the background-free scenario and the dashed line represents the presence of backgrounds. Figure from [34, 35].

- **High Detection Efficiency:** Germanium detectors can be highly enriched in ^{76}Ge , increasing the probability of capturing double beta decay events.
- **Signal-Background Discrimination:** Pulse shape discrimination (PSD) allows for the differentiation between signal and background events based on the shape of the detected pulses, further reducing background and increasing sensitivity to rare events [29].

LEGEND will be operated in two phases while scaling up the detector array mass. The initial phase (LEGEND-200) targets a detector mass of 200 kg of enriched ^{76}Ge , with a subsequent phase (LEGEND-1000) increasing the mass to 1000 kg [35]. This substantial increase in mass together with a reduction of background will significantly enhance the experiment's sensitivity to $0\nu\beta\beta$ in ^{76}Ge due to a higher exposure as seen in 3.1. With an sensitivity of 1.3×10^{28} years (99.7% CL) the inverted ordering neutrino mass scale would be fully covered [35].

3.2 LEGEND-200

The first stage of LEGEND started taking data in March 2023 at the underground facilities at the Laboratori Nazionali del Gran Sasso (LNGS) where the existing GERDA

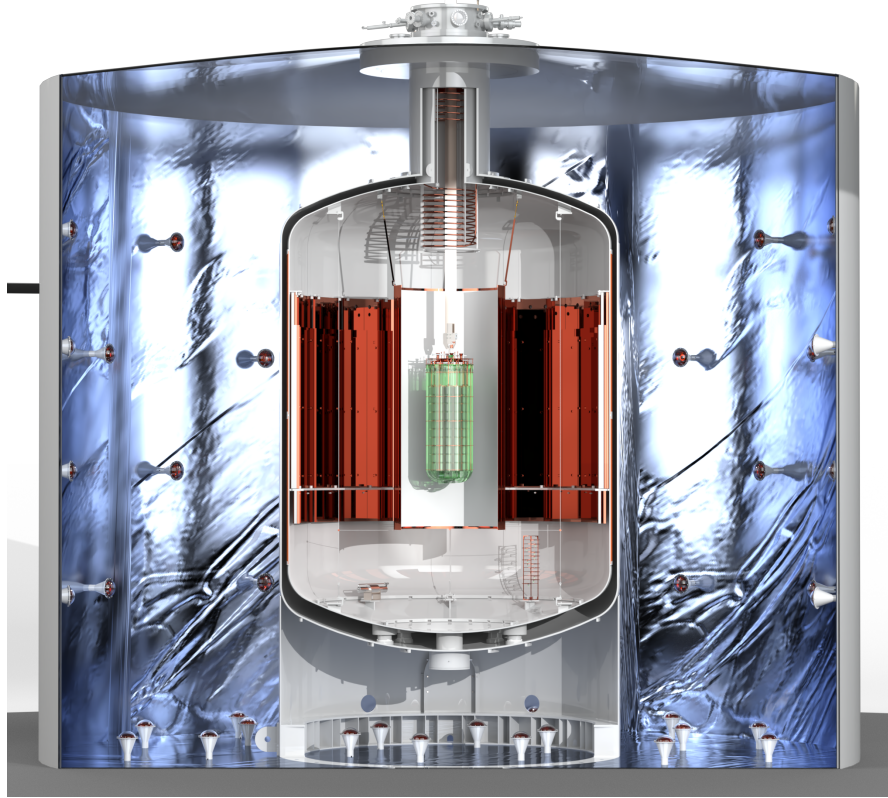


Figure 3.2: CAD rendering of the LEGEND-200 experiment setup. The detectors are arranged in strings, surrounded by wavelength-shifting fibers, and placed in the center of the Liquid Argon cryostat. Surrounding the cryostat is a water tank with the muon veto system. Image by Patrick Krause.

infrastructure is used. It will be operated for a duration of around years with up to 200kg of Germanium detectors to reach a target exposure of 1 t·yr. 4 different detector types are used, namely Coax, PPC, BeGe, and ICPC detectors. Their differences are explained in 2.3.2.

The experiment setup is sketched in 3.2. It consists of the HPGe detectors arranged in strings surrounded by wavelength shifting fibers. They are submerged into the liquid LAr cryostat containing the LAr system which itself is surrounded by water tank containing the muon veto. The LAr is used to cool the detectors but also to act as an active veto system.

The anticipated background index $B_{I,\text{tot}}$ in the region of interest for LEGEND-200 is $B_{I,\text{tot}} \approx 10^{-4}$ cts/(keV · kg · yr) with the different contributions listed in 3.3. The main source of these background are various different radioactive isotopes that decay and lead to energy deposition in the region of interest around $Q_{\beta\beta}$. Gamma backgrounds from ^{238}U and ^{232}Th can occur with $E_\gamma > 2$ MeV, where ^{208}Tl and

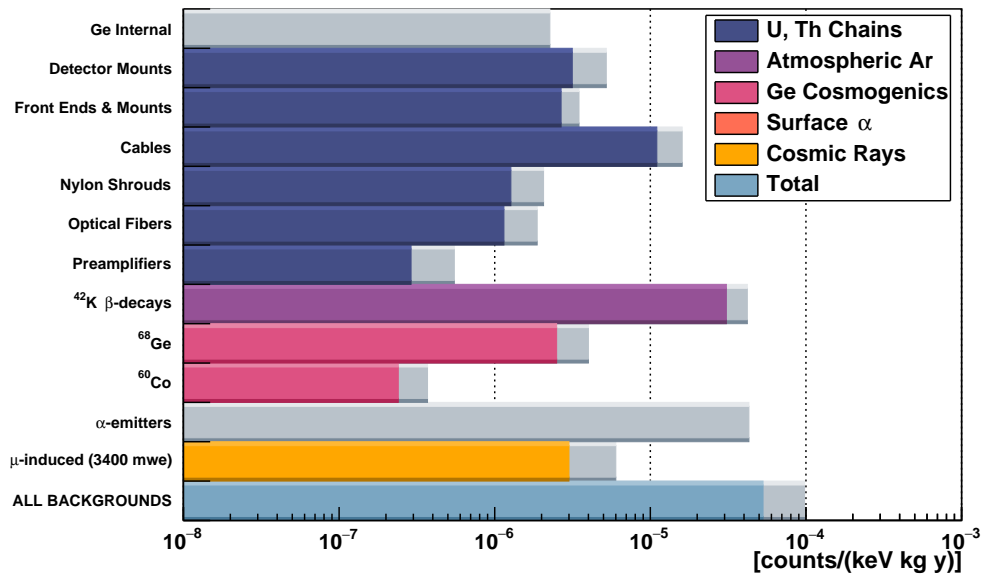


Figure 3.3: Projected backgrounds in LEGEND-200 are shown, with colored bars representing the estimated background contributions. Grey bars denote the 1σ uncertainties stemming from uncertainties in the screening measurements and Monte Carlo simulations. For uranium and thorium within germanium detectors, as well as alpha emitters on detector surfaces, only upper limits have been estimated. This plot is courtesy of the LEGEND collaboration.

^{214}Bi contribute to energy deposits within the signal ROI at the $Q_{\beta\beta}$ -value. Surface alpha events can originate from surface contaminations by ^{222}Rn and ^{210}Po . Additionally, surface beta events from the long-lived isotopes ^{42}Ar and ^{42}K in the n^+ contact can interfere with the $Q_{\beta\beta}$ ROI. Furthermore, cosmogenic activation by muons creates ^{68}Ge and ^{60}Co , which produce beta and gamma backgrounds in the ROI and can also generate low- and high-energy neutrons through interactions with rocks, leading to de-excitation and capture reactions.

To reduce background, various reduction strategies are deployed. These strategies are illustrated in Figure 3.4. The entire experiment is situated deep underground within the Gran Sasso massif, which provides shielding from cosmic radiation with an overburden of 3400 m.w.e. Muons that still penetrate the mountain can be detected by the muon veto system inside the water tank. Here, photomultiplier tubes detect Cherenkov light produced by the muons [37].

In the LAr system, Alpha and beta particles, gamma rays, neutrons, and muons deposit energy, producing scintillation light that is read out by silicon photomultiplier tubes (SiPMs) [37]. To reduce the loss of this scintillation light and enhance the veto efficiency,

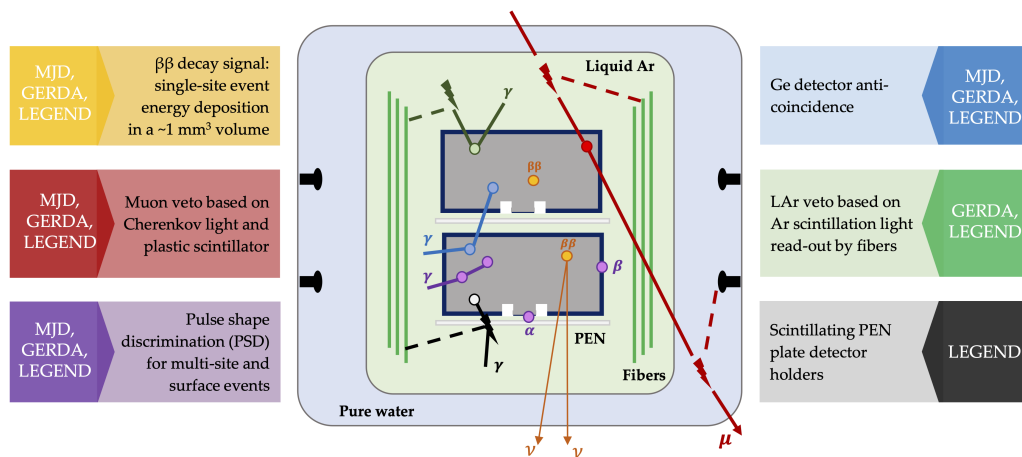


Figure 3.4: Illustration of the background reduction methods of LEGEND. The anticipated backgrounds can be largely mitigated using muon and liquid argon veto systems, along with scintillating materials like detector holders made from PEN. These techniques are complemented by analysis methods such as detector anti-coincidence cuts and pulse shape discrimination techniques to reject multi-site events, as well as alpha and beta surface events. Figure from [36].

different strategies are applied. For instance, wavelength-shifting fibers around the detectors capture any emitted light and guide it to the SiPMs. Additionally, baseplates made of scintillating material (PEN) and high-purity argon are used.

The use of ultra-clean materials further decreases background. Pulse shape discrimination also significantly contributes to lower the background index by background rejection, which will be discussed in the next chapter.

3.3 Data analysis

The Charge signals produced in the Germanium detectors are read out by the front-end electronics, where they are converted into a voltage signal, amplified and sent to the data acquisition (DAQ). It consists of FlashCam digitizers and an Object-orientated Real-time Control and Acquisition (ORCA) [38]. This system digitizes the signals from events, which are then stored for further analysis. Additionally, the liquid argon instrumentation and the muon veto generate substantial amounts of data that also require processing [32].

The LEGEND analysis processes all data to extract valuable physics information. It consists out of two software stack. The main software stack pygama is intended for the primary analysis and utilizes Python for the analysis [39]. The secondary software stack, JULEANA (JULIA LEGEND ANALYSIS), employs the Julia programming language and

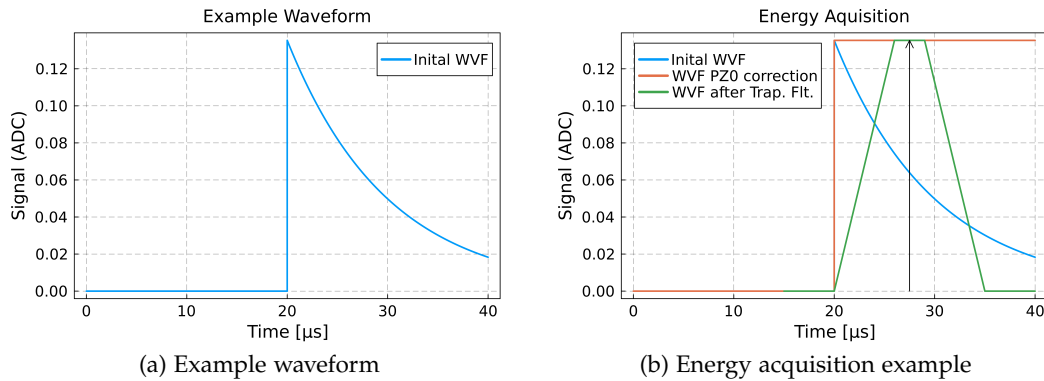


Figure 3.5: Plot of an ideal waveform (a) and the energy acquisition of it (b). The exponential decay tail is produced by the readout electronics. The exponential tail is fitted and compensated by a pole-zero correction. Then a trapezoidal filter is applied to the pole-zero corrected waveform and the energy is picked off in the middle of the filter.

serves as validation for the main software stack [40].

Although both software stacks differ in their details, they follow the same general procedure. First data from the DAQ is saved in binary, which is converted in HDF5 files. With the data in this format the waveform analysis is performed. During the Digital Signal Processing (DSP) physic parameters are extracted from the waveforms, e.g. the decay time constant of the waveform tail, the baseline value and slope, or the current. How the event energy is estimated will be explained in detail in 3.3.1.

With these DSP parameters, further analysis steps are performed, e.g. quality cuts, drift time corrections, or PSD, which will be discussed in 3.3.2. The final result is a energy spectrum of all events that passed the background cuts. With this the limit on $0\nu\beta\beta$ is calculated.

3.3.1 Energy reconstruction

Since the number of hole pairs created in the detector is proportional to the energy deposition, the signal height is also proportional to the energy. An example waveform for a signal can be seen in Figure 3.5a. These waveforms exhibit an exponential decay tail due to an RC-feedback loop in the front-end electronics, as further discussed in Section 5. A simple estimation of the signal maximum could involve taking the maximum of the waveform. However, this approach would yield an inaccurate value due to noise influencing the signal height and decreasing the energy resolution. Therefore, a more refined process is employed to determine the signal value, as illustrated in Figure 3.5b.

First, the exponential decay tail of the original waveform is fitted with an exponential function to estimate the decay time. Then, a pole-zero correction is applied to compen-

sate for the decay tail. This is done by applying an infinite impulse response filter to the waveform with the form [41]:

$$y[n] = y[n - 1] + x[n] - \alpha \cdot x[n - 1] \quad (3.1)$$

The result is the deconvolution $y[n]$ of the signal $x[n]$ at time $n = t$ with $\alpha = \exp(-1/\tau)$ as the deconvolution parameter.

A trapezoidal filter is subsequently applied to the pole-zero corrected waveform, and the energy is determined from the middle of the filter response. Depending on the specific detector, other filters may also be used; the one that achieves the best energy resolution is selected.

3.3.2 Pulse Shape Discrimination

While $0\nu\beta\beta$ decay is a localized phenomenon, where electrons deposit their energy within a small volume of $O(1 \text{ mm}^3)$ [11], gamma backgrounds can occur at multiple interaction sites due to Compton scattering. One powerful method to distinguish $0\nu\beta\beta$ between these events is pulse shape analysis (PSA) or pulse shape discrimination (PSD) [29]. While the energy of those events can be the same, their signal in the detector can look vastly differently. Figure 3.7 illustrates the distinct waveforms for different types of events. Because $0\nu\beta\beta$ events are SSE, the other event types can be recognized as background.

A common quantity for this discrimination is the ratio A/E , where E is the amplitude (energy) of the charge pulse, estimated as described in 3.3.1, and A is the maximum amplitude of the current pulse, which is the derivation of the charge pulse. The A/E distribution for SSEs is narrow and slightly energy-dependent (see Fig. 3.6), while for MSEs, it is broad and at lower values due to reduced maximum current amplitude. This also applies to n^+ surface events, where initial charge diffusion causes longer charge collection times compared to normal bulk events, resulting in characteristic low A/E values. Events near the p^+ contact exhibit high A values, resulting in $A/E > 1$.

In LEGEND, ^{228}Th calibration runs are used to define A/E cuts. ^{208}Tl , one of its daughter nuclei, produces 2614.5 keV gammas. This energy is high enough to allow pair production (see 2.4.2), therefore producing a FEP at 2614.5 keV, a SEP at 2103.5 keV, and a DEP at 1592.5 keV. The cut on the A/E value is then tuned to let 90% of the DEP survive, as shown 3.7. Events outside of this window are subsequently cut as background events.

A/E is a highly effective tool for rejecting multi-site events by eliminating events that fall below the SEE band. Cutting events above the SEE band primarily removes alpha surface events. While for some detectors, this high A/E cutting method is optimal, other techniques can also be effective. In detectors with large passivated surfaces like PPC detectors, the Late Charge (LQ) cut surpasses the high A/E cut in efficiency for

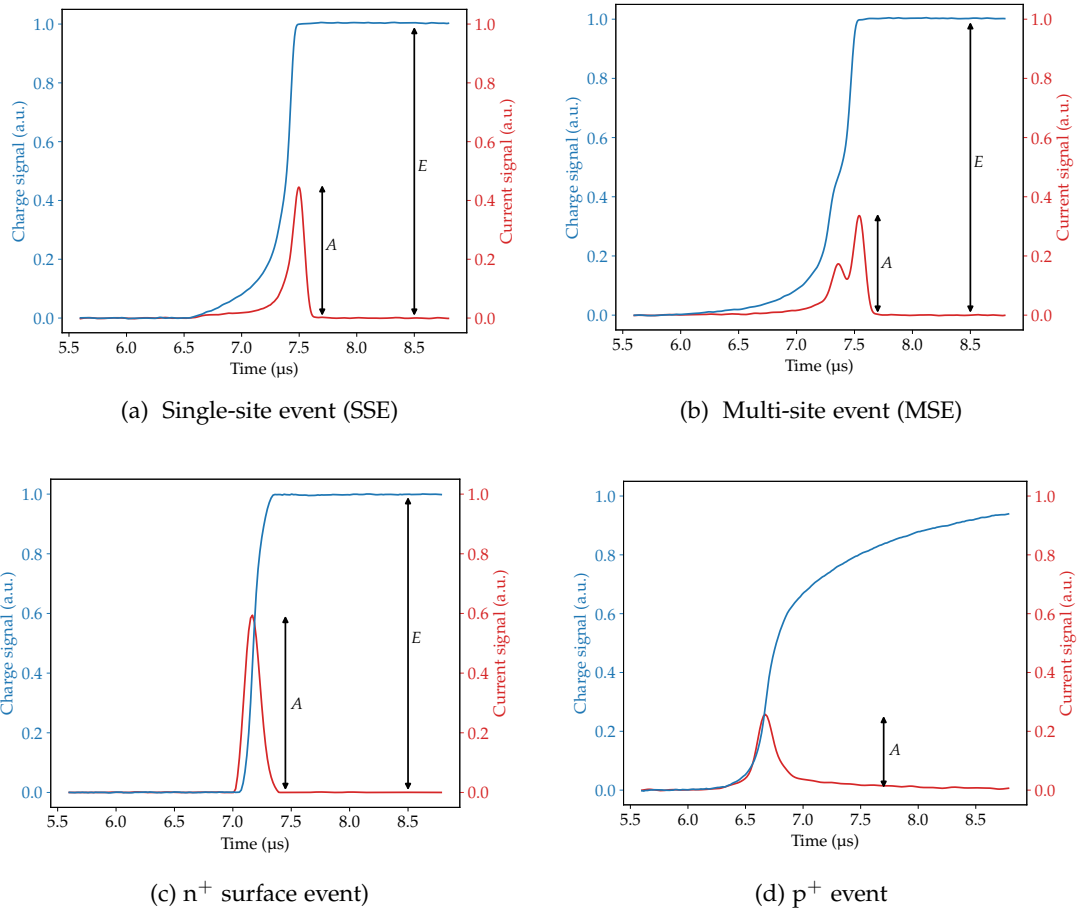


Figure 3.6: Single-site event, multi-site event, n^+ surface event, and p^+ event with their respective charge (blue line) and current (red line) signal. Figures from [11]

removing alpha surface events. The mechanism and implementation of this cut in JULEANA will be explained in section 4.

3.4 LEGEND-1000

The LEGEND-1000 project represents the second phase of the collaboration, planned to be built at LNGS and expected to begin data collection around 2030. The project aims to operate 1000 kg of Germanium over a span of 10 years to achieve a total exposure of 10 t-yr. To accomplish this, 400 ICPC detectors, each with an average mass of 2.6 kg, will be deployed. This section gives an short overview of the LEGEND-1000 concept, more detail can be found in [35].

The currently planned layout for the experiment is illustrated in Figure 3.8. Similar

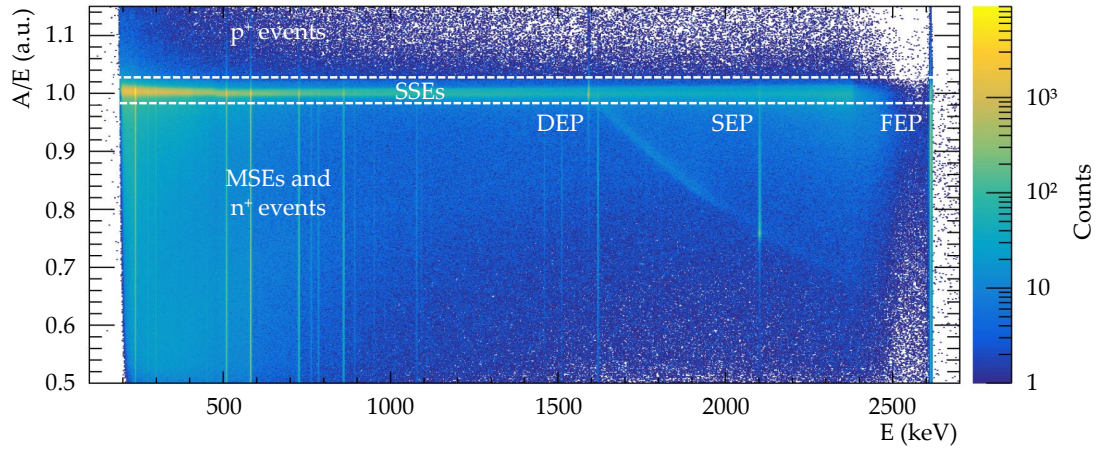


Figure 3.7: The normalized A/E distribution for a ^{228}Th calibration run as a function of energy, with the single-site event (SSE) band centered around $A/E = 1$. Multi-site events (MSEs) and n^+ surface events have $A/E < 1$, while events near the p^+ contact exhibit $A/E > 1$ Figure from [11].

to LEGEND-200, the detectors will be deployed in strings surrounded by wavelength-shifting fibers submerged in liquid Argon (LAr). However, unlike LEGEND-200, the liquid argon cryostat in LEGEND-1000 will be split into two parts. The inner re-entrant tube, where the detectors are located, will be made from ultra-pure electroformed copper and filled with Underground Argon (UG LAr). UG LAr is extracted from deep underground mines, in contrast to conventional argon, which is liquefied from the air. This is advantageous because UG LAr contains fewer cosmogenically activated isotopes, such as ^{39}Ar and ^{42}Ar , which would otherwise increase the background. The outer part of the cryostat will be filled with atmospheric argon and equipped with a neutron moderator. The LAr instrumentation will include SiPMs installed throughout the entire cryostat. Additionally, the cryostat will be surrounded by a muon veto system.

The collaboration plans to further decrease the background by one order of magnitude compared to LEGEND-200:

$$B_I < 1 \cdot 10^{-5} \text{ cts}/(\text{keV} \cdot \text{kg} \cdot \text{yr}) \Leftrightarrow B_I < 0.03 \text{ cts}/(\text{FWHM} \cdot t \cdot \text{yr}) \quad (3.2)$$

The individual components are listed in 3.9. With this background index and exposure the discovery sensitivity on the half live will be $T_{1/2}^{0\nu} > 10^{28} \text{ yr}$ [35]. This would fully cover the regime of inverted mass ordering, see 3.1 and 1.5.

To achieve the ambitious background reduction goals, additional techniques are necessary. With the exclusive use of ICPC detectors, surface alpha backgrounds can be significantly reduced. These bigger detectors allow for PSD like the PPC and BeGe

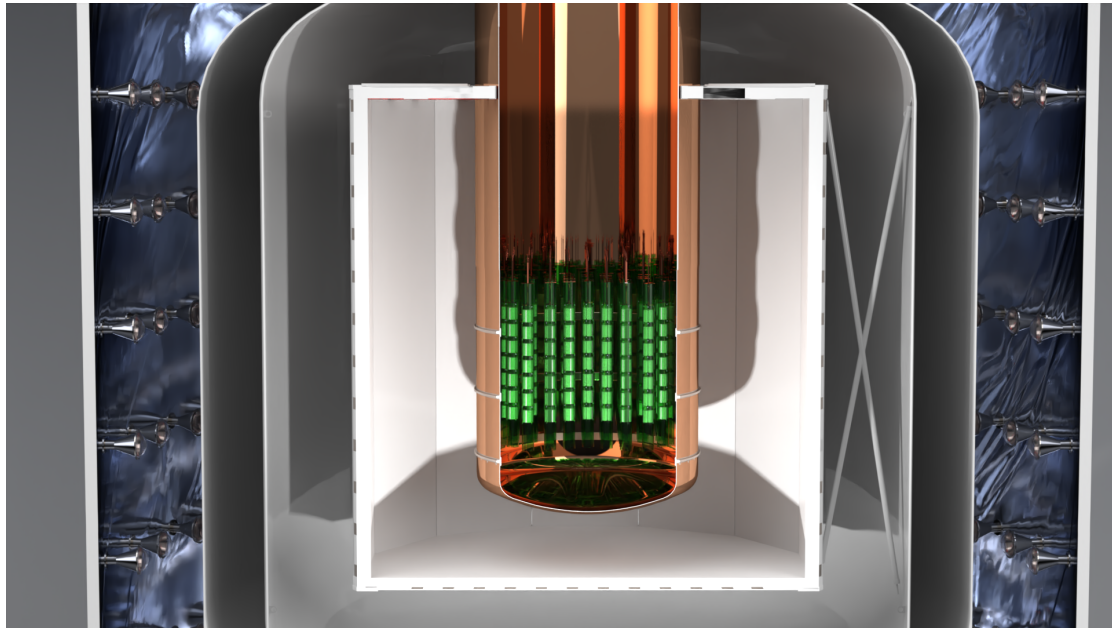


Figure 3.8: CAD rendering of the LEGEND-1000 experiment setup. In contrast to LEGEND-200 the LAr cryostat is split in two parts. The tube containing the detectors is filled with underground Argon while the outer part uses atmospheric argon. In the outer part a neutron moderator is added. The cryostat is again surrounded by a muon veto. Image by Patrick Krause.

detectors [42], and also have the advantage to reduce electronics as compared to many more smaller detectors. Additionally, the background from the radioactive decay of ^{42}K can be mitigated by using underground liquid argon (UG LAr). Extracted from deep mines, UG LAr has low levels of the isotope ^{39}Ar and likely ^{42}Ar as well. Alternative strategies are also being considered, such as increasing the thickness of the lithiated n^+ electrode or using PEN encapsulation for the HPGe detectors.

Another approach to further reduce backgrounds involves optimizing the signal readout electronics. The baseline design for LEGEND-1000 includes the use of a custom-designed application-specific integrated circuit (ASIC) readout scheme. ASIC technology allows the integration of the entire charge-sensitive amplifier (CSA) into a single low-mass chip, while maintaining the spectral and noise performance of conventional solutions [43]. One of the main objectives of this work is to demonstrate the feasibility of operating a large-scale germanium detector with a readout ASIC. More details on the development of signal readout electronics for LEGEND-1000 are discussed in Chapter 5.

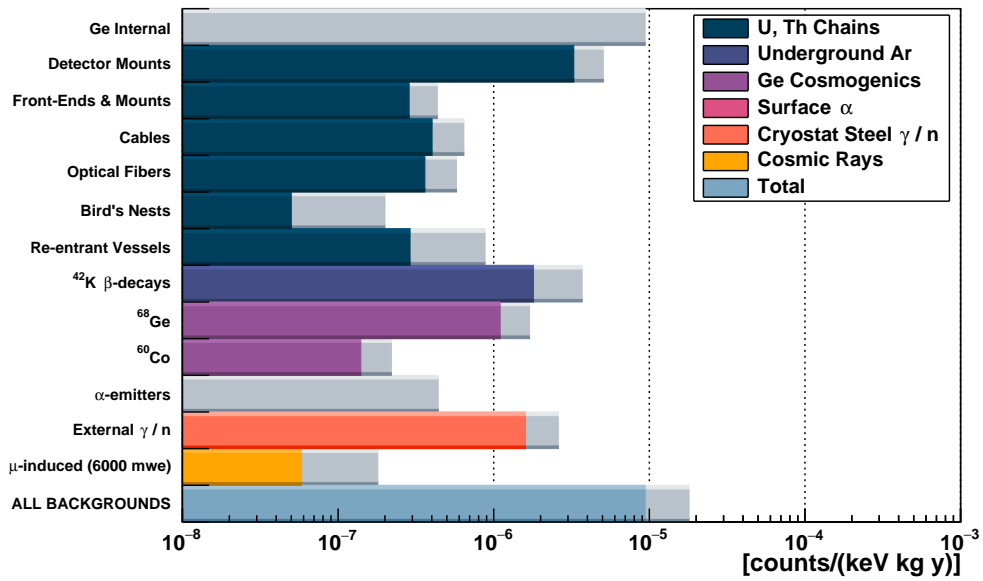


Figure 3.9: Projected backgrounds in LEGEND-1000 are shown, with colored bars representing the estimated background contributions. Grey bars denote the 1σ uncertainties stemming from uncertainties in the screening measurements and Monte Carlo simulations. For uranium and thorium within germanium detectors, as well as alpha emitters on detector surfaces, only upper limits have been estimated. This plot is courtesy of the LEGEND collaboration.

Chapter 4

Implementation of the Late Charge cut for the Juleana Analysis

As mentioned in chapter 3.3.2 pulse shape discrimination is an important tool for the analysis of Germanium detectors to remove background events. One of the parameters used in PSD is the Late Charge (LQ), whose implementation into the JULENA analysis will be explained in this chapter.

4.1 Motivation of the LQ-cut

LQ is used as the key parameters used to eliminate background caused by α and β -decay surface events, as well as certain multi-site events. This chapter will discuss the background events that the LQ parameter targets for exclusion, and it will highlight the advantages of LQ compared to other PSD parameters.

4.1.1 Surface background sources

One of the major background components in LEGEND are alpha events especially from decays within the ^{222}Rn decay chain [11]. In the Radon decay chain ^{210}Pb accumulates, due to its long lifetime of $T_{1/2} = 22.2\text{yr}$ when compared to other isotopes in the chain [44]. While ^{210}Pb decay via β -decay, the subsequent decay of ^{210}Po is critical due to it releasing an alpha particle with energy of $E_\alpha = 5407.5\text{ keV}$ [44]. Radon, a noble gas, naturally occurs in the Uranium and Thorium decay chains. During detector manufacturing, a slight surface contamination is unavoidable. Additional contamination may result from radon outgassing of parts close to the detector, contributing to undesired background events.

β -decay events are mainly expected to originate from the decay of ^{42}K into ^{42}Ca , which produces betas with energies of up to $E_\beta = 3525.4\text{ keV}$, which is higher than $Q_{\beta\beta}$ [44].

^{42}K is the progeny of ^{42}Ar , which is naturally abundant in liquid argon (LAr) and produced through cosmogenic activation. In the LAr volume, K^- ions are attracted to the n^+ electrodes, and accumulate there [45].

4.1.2 Germanium detector surface effects

Both alpha and beta events don't reach deep into the bulk of the detector and deposit their energy close to the surface of the detector. Depending on where exactly this energy deposition takes place, the signal shape of the waveforms changes in comparison to an event in the bulk.

The n^+ contact of Germanium detectors is a few millimeters thick thus, alpha particles cannot penetrate it and do not produce a background, whereas beta events lead to slow pulses. Simulations suggest that this is the effect of slow charge diffusion from the transition layer into the bulk [46]. The p^+ contact is usually thinner and only $0.3\ \mu\text{m}$ thick which means also alpha events reach the active volume and produce a signal [45]. These signals near the point contact produce a distinct pulse shape with sharp rising edge.

Additionally detectors can have passivated surfaces made from amorphous germanium to separate the n^+ and p^+ contact, in particular PPC detectors large ones. Since this passivation layer is left floating, i.e. its electric potential is undefined, charge can accumulate on it, altering the electric field around it and affecting the drift paths of holes and electrons [45]. If the surface is negatively charged, holes created by interactions near the detector surface are attracted to the passivated surface, causing them to drift very slowly towards the point contact. This can lead to an incomplete charge collection within the signal formation time, and lead to them not contributing to the signal. For a positively charged surface, electrons are similarly affected as the holes for a negative surface.

These effects cause alpha events to produce a phenomenon observed in Germanium detectors called Delayed Charge Recovery (DCR), where the tail of the waveform is modified by a delayed charge component. This process is not fully understood but there are two different explanations for this phenomenon [45]. The origin could either be charge trapping near the passivated surface and a slow re release of the charges into the bulk material, or charges drifting close to the passivated surface, having their mobility massively reduced [47]. The observed waveform is illustrated in Figure 4.1, which compares alpha and gamma pole-zero corrected waveforms. While the gamma event waveform slope remains flat, the alpha event waveform shows a rising component in its tail. Identifying this feature can be an effective method for removing surface alpha events [45].

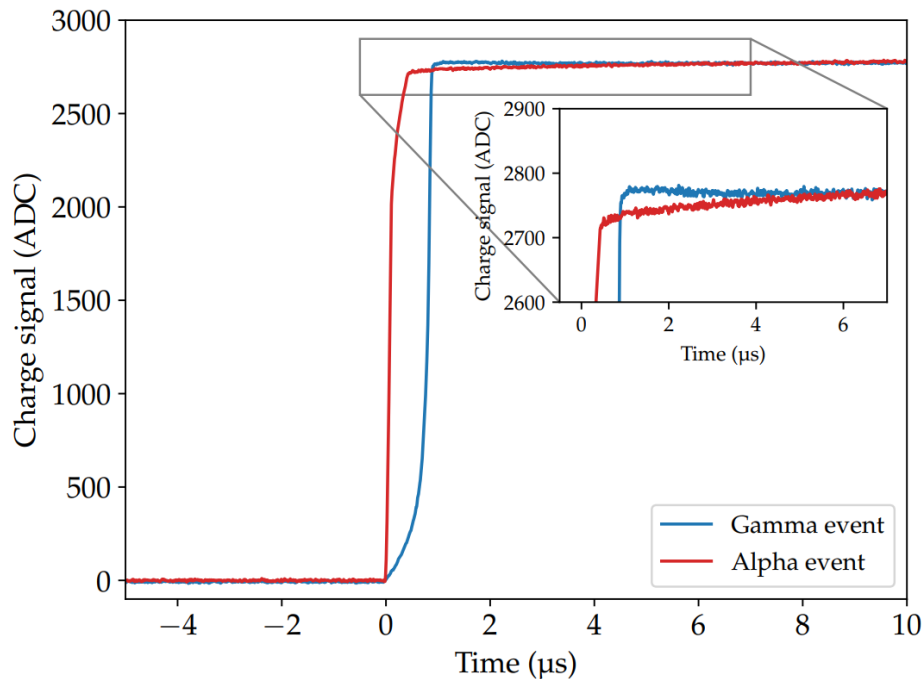


Figure 4.1: Pole-zero corrected waveforms for a bulk gamma event(blue) and surface alpha event(red). A slow rising component can be seen in tail of the red waveform, which can be explained by the DCR phenomenon. Figure from [45]

4.1.3 Advantages of the LQ cut

As explained in section 3.3.2, the A/E value is one of the PSD parameters for PSD. While it is great tool to distinguish multi-site from SSE events and can also be used for surface events in the contacts of the detector, it also has some drawbacks. For A/E identifying SEE events correctly the weighting potential of the detector needs to be the same at the regions where the particles interact. If this is not the case, the normally lower current signal of an MSE can be modified to wrongly match the one of an SSE. The high A/E cut is used to reject these surface events. While the method is effective for events close to the contact it is not for events events farther away. Also DCR events can't be easily distinguished from SSE events because their currents are similar.

To aid the A/E parameter in the PSD other parameters that rely on a different signature than A/E than u can also be very usefully. LQ compares the charge waveforms at the top part of their rising edge, where the waveform reaches 80% of its maximum. Background events that distort the waveform in that region change the LQ parameter, which allows their detection. The LQ parameter can be used to catch the multi-site events that the A/E does not cut, as they produce kink at the top of the rising edge. Additionally LQ is sensitive to the DCR events as they also would change the LQ parameter. Especially for PPC detectors where these events are more frequent than for

other detectors, it can be advantageous to use an LQ cut instead of an high A/E cut. For the LEGEND analysis the efficiency of these two cuts needs to be compared for each detector and the one performing better will be chosen for the analysis.

4.2 LQ cut implementation in JULEANA

As mentioned before the LQ is a powerful tool in PSD that can help to identify and reject background events. The next chapter will discuss how the cut was implemented into the JULEANA analysis, its working principle and its performance. For this analysis the Thorium calibration runs in p03 of the LEGEND-200 data are used. During these runs 4^{228}Th sources with a activity of a few kBq are lowered into into the LEGEND cryostat and calibration data is taken for 4 hours [38].

4.2.1 Parameter extraction

The LQ parameter analyzes the shape of the waveform at the end of its rising step. It is defined as the difference of two integrated waveform areas in ranges of $2.5\mu\text{s}$. The first area starts where the pole-zero corrected waveform reaches 80% of its maximum (t_{80}), while the second area begins where the first one ends. These two areas are visualized by the blue and green areas in Figure 4.2.

Since the blue area starts at 80% of the waveform's maximum, LQ is sensitive to changes in the last 20% of the waveform's rising edge. The surface effects mentioned in section 4.1.2 can modify the signal shape in this region, typically increasing the LQ area. For instance, the slow-rising component during DCR events would lead to an increase in the LQ parameter (visible in the zoom of Figure 4.1). Additionally, multi-site events that create a kink at the very end of the waveforms rising edge, can be identified by the increase of the LQ area, as shown in Figure 4.2.

4.2.2 Raw LQ corrections

To compare different events by their LQ value, the raw LQ value needs to be corrected and normalized to account for differences created by differences in energy or drift time.

Energy correction

Figure 4.3a shows the raw LQ parameter of one PPC detector for all thorium calibration runs in period 03 plotted against their energy. A linear correlation between energy and LQ can be observed. This is caused by the waveforms having larger ADC values for higher energies, resulting in larger LQ values. To account for this, the raw LQ parameters are divided by their uncalibrated energies. This removes the energy dependence as visible in Figure 4.3.

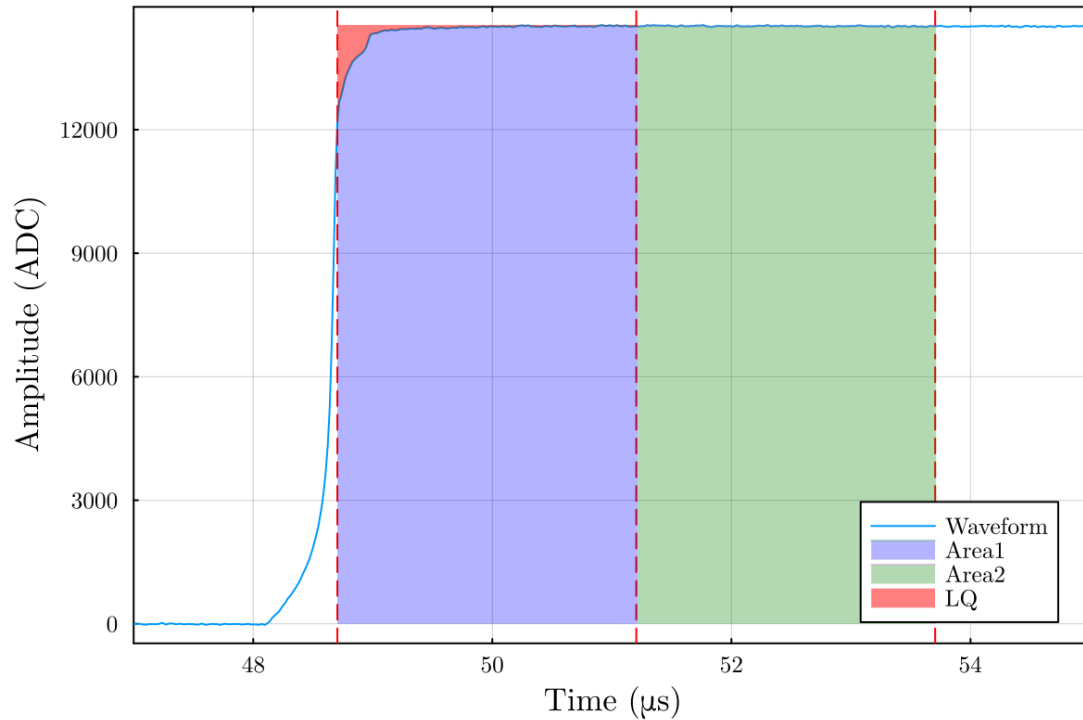


Figure 4.2: Example LQ parameter acquisition for a multi-site event waveform. The raw LQ value is defined as the difference between the blue and green areas. The blue area starts at the time when the waveform reaches 80% of its maximum and spans 2.5 μs .

Drift time Correction

Events with longer drift times have a longer path to the readout electrode. During this travel, the charge cloud increases in size due to the repulsive forces between like charges as well as diffusion into the surrounding material [48]. Consequently, identical events can have different LQ values depending on their position in the detector. This effect can broaden a monoenergetic peak. Therefore, a correction is necessary.

The charge trapping correction is tuned on the DEP of the ^{208}Tl peak in the Thorium calibration runs. The DEP events from one detector during a run are shown in Figure 4.4a, where the distribution of LQ vs. drift time is plotted. The events mainly populate a single cluster, indicating a linear dependence where events with longer drift times have higher LQ values.

To estimate a correction, outlier events from the main cluster are first excluded. Then, a linear function is fitted through the remaining events. This linear function is used to correct the LQ parameters for drift time.

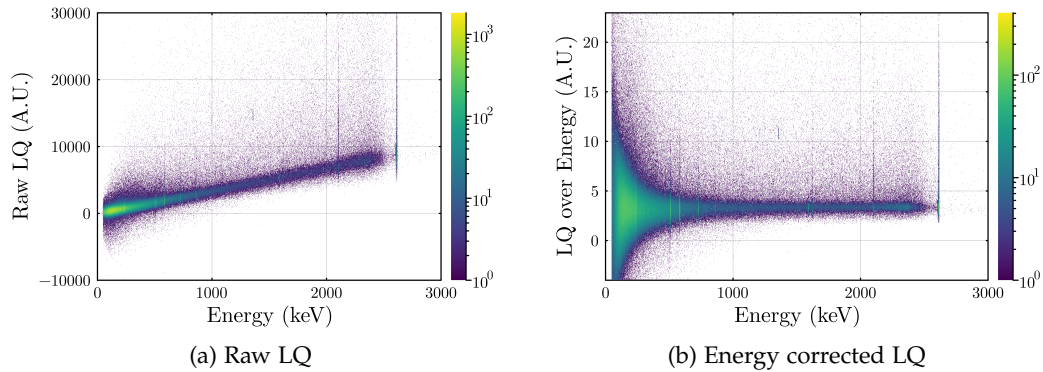


Figure 4.3: 2D histogramm of the a) raw LQ parameter and b) LQ after energy correction from all calibration runs of period 3 of one detector. The raw LQ parameter shows a linear energy dependence with higher LQ for higher energies. After the energy correction the LQ value of the main band shows no longer a energy dependence.

ICPC detectors

ICPC detectors exhibit a slightly different LQ distribution, characterized by two clusters instead of one. The linear trend of higher drift times corresponding to higher LQ values is still visible. The correction routine is similar to that used for other detectors, involving fitting a linear function through the DEP events after removing outliers. Figure 4.4b shows the fit function and the box indicating the events used for the fit.

LQ classifier

After the corrections we get the LQ classifier, which is plotted in figure 4.5. This corrected LQ parameter is then used to tune the cut and identify the background events

4.2.3 Final cut estimation

To estimate the cutoff value for the LQ cut, the signal-like events in the DEP are used. Since the energy region of the DEP also contains background events, these need to be subtracted. For this purpose, three regions are defined:

- Region 1: $[\mu_{\text{DEP}} - 2 \cdot 4.5\sigma, \mu_{\text{DEP}} - 1 \cdot 4.5\sigma]$ (left side band)
- Region 2: $[\mu_{\text{DEP}} - 1 \cdot 4.5\sigma, \mu_{\text{DEP}} + 1 \cdot 4.5\sigma]$ (peak region)
- Region 3: $[\mu_{\text{DEP}} + 1 \cdot 4.5\sigma, \mu_{\text{DEP}} + 2 \cdot 4.5\sigma]$ (right side band)

For each energy region a histogram in the LQ distribution is created, as shown in Figure 4.6a. The sideband histograms containing only background events are then subtracted from the peak region histogram. This resulting histogram is fitted with a Gaussian distribution, as depicted in Figure 4.6b.

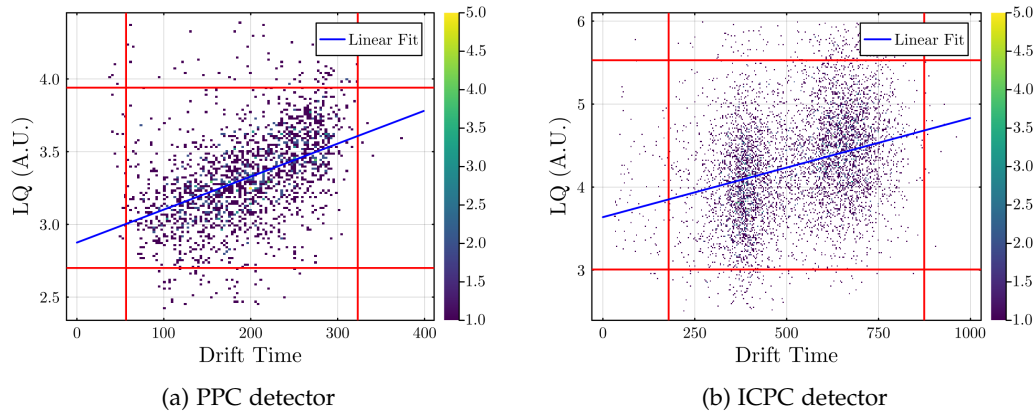


Figure 4.4: Distribution of LQ vs. drift time for DEP events in a) a PPC detector and b) a ICPC detector. The events outside the red box are not used for drift time correction. The events side inside the red box a fitted with a linear function. While the events in the PPC detector are in a single cluster, for the ICPC detector two clusters are visible

The cut-off value for the LQ cut is then defined as 3σ of the Gaussian fit of the side band subtracted DEP histogram. All events that have an higher LQ classifier than the estimated value are cut. This is visualized in Figure 4.7a. An example of an waveform excluded by the LQ cut is shown in 4.7b as well as an waveform surviving the cut. They were shifted so that their t_{80} values overlap. It is visible that the cut waveform has a lower signal than the uncut Waveform, which increases the LQ classifier and is the reason it got excluded by the LQ cut. This shows that with the LQ classifier background events can be identified and successfully rejected.

4.2.4 Performance and conclusion

To test the LQ cut, the ^{208}Tl peaks from the Thorium calibration are analyzed. A useful measure is the survival fraction, which is estimated by fitting the peaks before and after applying the cut, and then dividing the background-subtracted peak counts before and after the cut. For the DEP, it is expected that most events will pass ($>99\%$), while a higher percentage of other peaks will be cut. This evaluation is illustrated for one PPC detector in Figure 4.8. As expected the DEP events have a very high survival fraction or different cu values, while for the other peaks, as well as the $Q_{\beta\beta}$ compton continuum region more events are cut. This is due to the multi site events that get excluded by an high LQ classifier.

Figure 4.9 shows the survival fraction of events in the DEP after the LQ cut was applied for different detector types used in LEGEND-200. It is visible that the performance of the cut depends on the detector type. While the survival fraction for BEGe detectors is the lowest, it's highest for PPC detectors. This means that more events of DEP are cut for BEGe detectors than for PPC detectors.

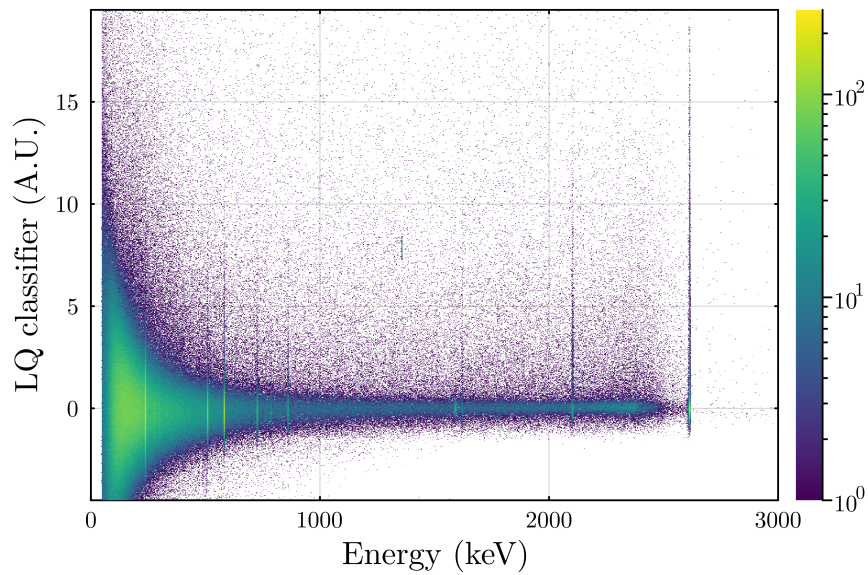


Figure 4.5: 2D histogram of the LQ classifier vs Energy. The plots shows one main band centered around 0 where most of the events are. In this region bulk waveforms with no special LQ distortion are situated. Background events increase the LQ classifier and are situated above the main band.

These plots show that a first implementation of the LQ cut into the JULEANA analysis was successful. To evaluate its performance it needs to be compared to the performance of the A/E cut to see if the LQ cut is able to cut events that are missed by the A/E cut and therefore useful to be included into the analysis. This work highlighted the first version of the LQ cut analysis in JULEANA, but there are still several ideas for optimizations that need to be investigated to improve the effectiveness of the LQ cut. Additionally comparisons to the LQ cut implementation in the other software stack pygama should be made as a crosscheck for both teams.

Since these surface effects are also not fully understood, simulations could be made to simulate the expected survival fraction the LQ cut should produce, when background events are cut by it. These simulation then can be used to see if the experimental LQ cut effectiveness matched the expectations from the simulation.

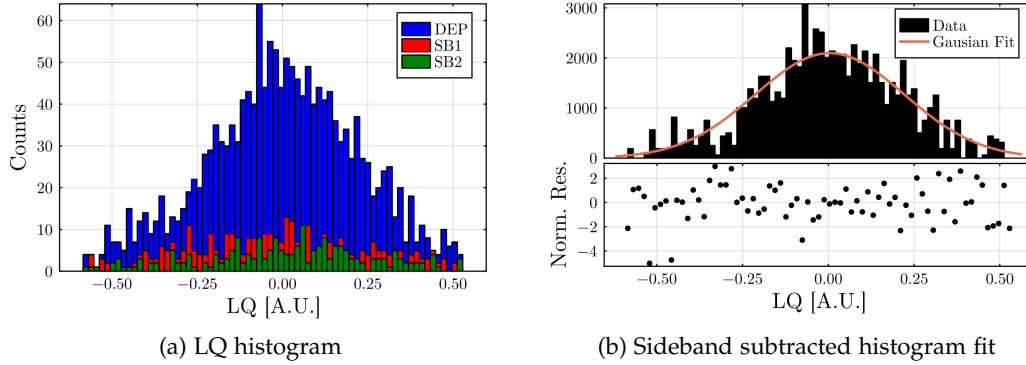


Figure 4.6: Figure (a) shows the histograms of LQ counts for the DEP and the two side bands next two it, used to create the side band subtracted. The sideband, subtracted DEP histogram is shown in Figure (b) where a Gaussian fit of the side band is performed. The normalized residuals are shown below.

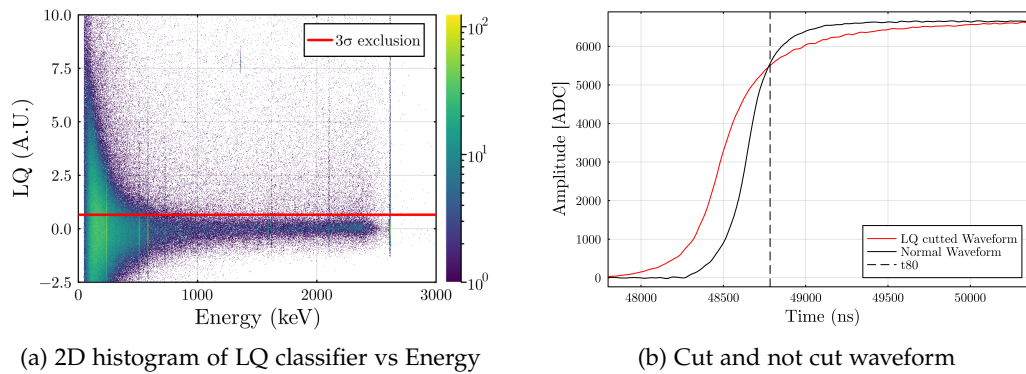


Figure 4.7: Figure (a) shows a 2D histogram of LQ classifier vs Energy. The red line marks the LQ cut cutoff value of 0.643. Events above this line are excluded with the LQ cut. One waveforms that gets cut(red) and one that does not get cut(black) are plotted in figure (b), together with their t_{80} . Its visible that the cut waveform has a lower signal than the uncut Waveform, which increases the LQ classifier and is the reason it got cut.

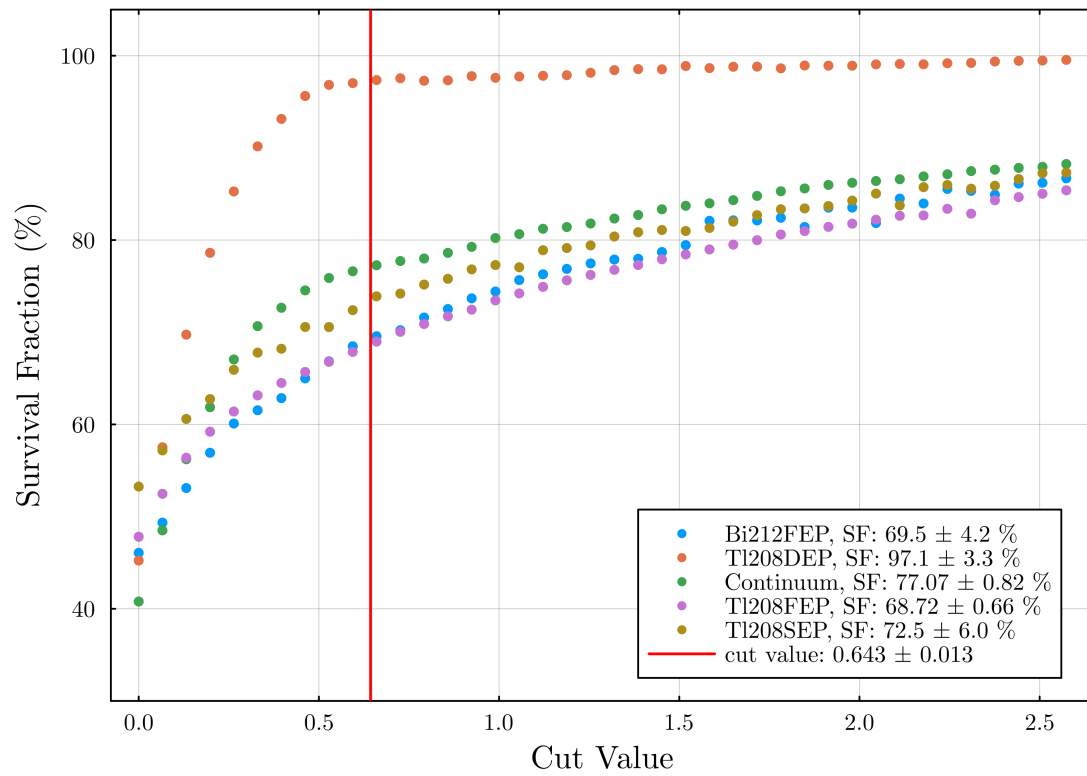


Figure 4.8: Survival fraction of one PPC Detector for Different LQ cut values. The different peaks are represented with different colors

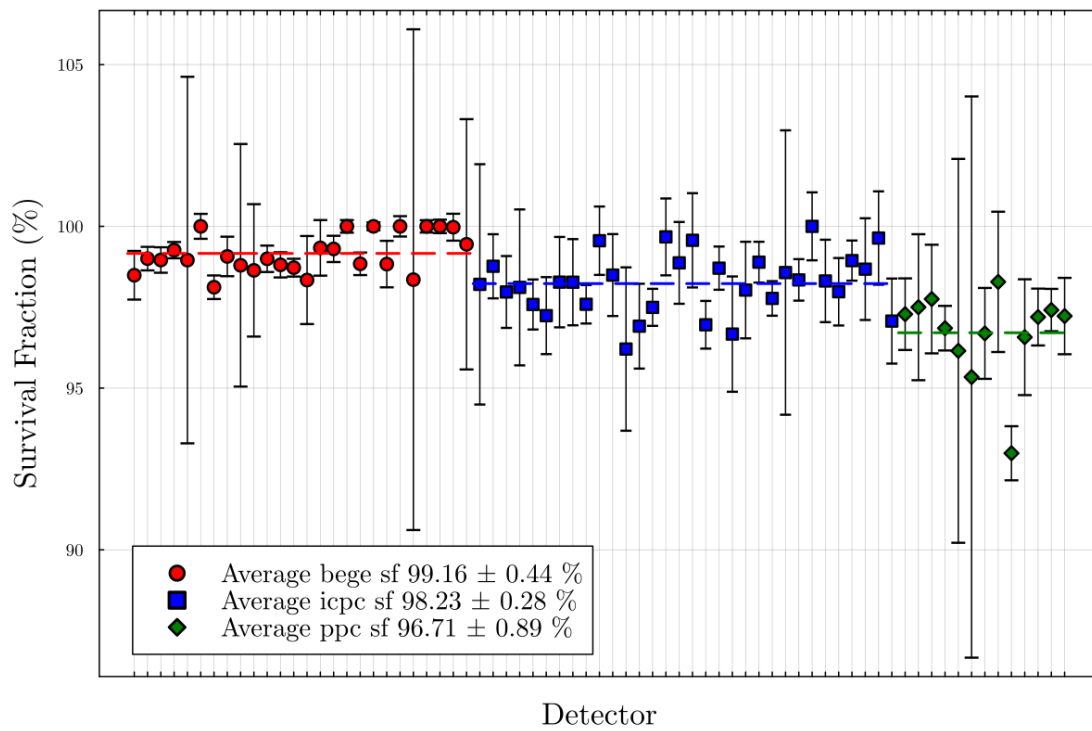


Figure 4.9: Survival fraction with uncertainty of events in the DEP after the LQ cut for each detector in the calibration runs of LEGEND-200 period 3. The three different detector types PPC(green), ICPC(blue) and BEGe(red) differ in their average of Survival fraction(dotted lines).

Chapter 5

Results from the first iteration of the ASIC-based readout system LUIGI

Efficient signal readout electronics are crucial for enhancing the sensitivity of germanium detectors by minimizing electronic noise and refining pulse shape analysis (PSA) for effective background rejection. However, placing these electronics near the detectors requires them to be as radio-pure as possible. To improve the current readout electronics used in LEGEND-200, ASIC technology is investigated. One approach is the LUIGI (LEGEND Ultralow background Integrated circuit for Germanium detectors Investigations) ASIC, whose initial results will be discussed in this chapter.

5.1 Signal readout electronic for LEGEND-1000

To process the signals generated by particle interactions within the HPGe detector, they first need to be converted from a charge signal into a voltage signal. Also they are very small and difficult to be processed. To address this, charge-sensitive amplifiers (CSA) are used to convert these signals and amplify them, allowing them to be read out by an DAQ system.

5.1.1 CSA working principle

A simplified version of a charge-sensitive amplifier is illustrated in Figure 5.1. When the detector is reversed biased with high voltage it behaves electronically as a diode with a capacitance C_D . The charge produced by an event in the detector is collected and integrated over a capacitor C_f . The voltage is then amplified by a combination of a junction-gate field-effect transistor (J-FET) and an operational amplifier (OpAmp). The J-FET is needed to counter the slow loading of the OpAmp and acts as a current source to produce higher cutoff frequencies and increase the band width. This allows for the processing of faster signals without disturbing the signal shape, which is crucial

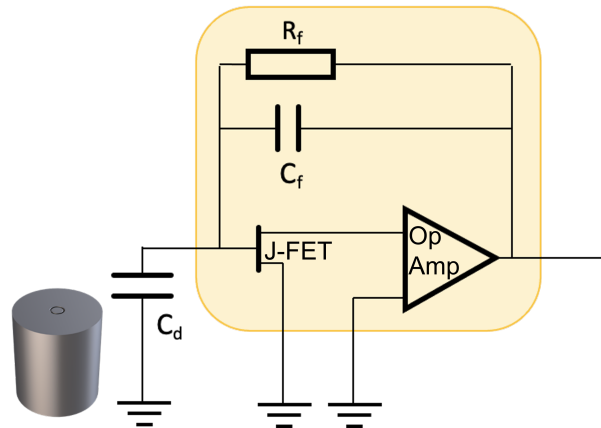


Figure 5.1: Simplified circuit for a charge sensitive amplifier. The charge of an signal is integrated over a capacitance C_D , and amplified via the OpAmp and J-FET. The charge on the capacitance is continuously drained over an resistor R_f . Scetch by Florian Henkes.

for PSD cuts during data analysis. To prevent the capacitor from saturating during operation, it needs to be discharged, which is achieved via a resistor R_f , placed in parallel. This results in an exponential decay tail in the waveform with a time constant τ :

$$\tau = R_f C_f \quad (5.1)$$

For $0\nu\beta\beta$ -decay searches, it is crucial to minimize noise that degrades energy resolution. To achieve this, the CSA should be positioned as close as possible to the detector [49]. Additionally, extending the system's bandwidth allows for faster signal rise times, facilitating PSD cut techniques. However, this is countered by the fact that materials placed near the detector can introduce radioactivity, increasing backgrounds. Therefore, it is essential to minimize the amount of material used and ensure it is as radiopure as possible [50]. A compromise between background reduction and electronic performance is thus required.

Furthermore, the CSA must meet several additional requirements. It needs to operate at cryogenic temperatures, endure multiple cooling cycles without breaking, be compatible with different detector capacities, resist Electro Static Discharge (ESD) damage during detector installation, and transmit a signal to the DAQ system without excessive power consumption, since this could lead to local boiling of the liquid argon.

5.1.2 Electroic Noise

Electronic noise is an unwanted disturbance in a electronic signal. In the case of a CSA, it can mask important information of the signal (e.g. interfere with the rising edge used in PSD) and lead to in accurate measurement of charge. This worsens the energy

resolution degrading the ability to distinguish background events from $0\nu\beta\beta$ events near $Q_{\beta\beta}$. Two main effects contribute to the total electronic noise [51]:

- Random fluctuations of the charge carrier velocities due to thermal motion
- Random fluctuations of the charge carrier number

Typically electronic noise is expressed by equivalent noise charge (ENC). It corresponds to the amount of charge (number of electrons) that when injected into the CSA produces a signal-to-noise equal to one. To the total ENC value three uncorrelated components are contributing, which are the parallel noise ENC_p , the series noise ENC_s , and the $\frac{1}{f}$ noise $ENC_{1/f}$ [52]:

$$ENC^2 = ENC_p^2 + ENC_s^2 + ENC_{1/f}^2 \quad (5.2)$$

The parallel noise ENC_p^2 is driven by the detector leakage current I_D and the thermal noise induced by the feedback resistor R_f and can be expressed as [51]:

$$ENC_p^2 \propto \left(2eI_T + \frac{4k_B T}{R_f} \right) \tau_s \quad (5.3)$$

Here, $I_T = I_D + I_G$ describes the total current consisting of the leakage current and gate current I_G of the J-FET, k_B the Boltzmann constant, T the operational temperature of the feedback resistor, and τ_s a characteristic shaping time of the selected shaping filter.

Sources in series with the detector signal produce the series noise ENC_s . The main component originates from shot noise in the JFET. It can be expressed as [51]:

$$ENC_s^2 \propto \frac{4k_B T}{g_m} \frac{C_T^2}{\tau_s} \quad (5.4)$$

where g_m is the transconductance of the J-FET, and C_T the total capacitance, which is sum of Detector capacitance C_D , input capacitance C_i of the CSA, and the feedback capacitance C_f [52]:

$$C_T = C_D + C_i + C_f \quad (5.5)$$

Since usually the detector capacitance is the dominating contributor [53], Detectors with a low capacitance are preferred.

$ENC_{1/f}$ is the $\frac{1}{f}$ noise, which is independent of the shaping time and is usually subdominant [54]. It can be expressed by [51]:

$$ENC_{1/f}^2 \propto A_f C_T^2 \quad (5.6)$$

Here, A_f describes a noise factor that depends on the dielectric properties and the fabrication process of the specific JFET [55].

Since the the parallel noise has a τ_s and the series noise a $\frac{1}{\tau_s}$ component there exist and optimal shaping time that minimizes the ENC value. Therefore it is crucial for the data analysis to find the optimal shaping time for any chosen shaping filter to minimize the noise [56]. Minimizing the ENC value is crucial to gain the best energy resolution, because ENC is influencing the energy resolution. Its contribution to the FWHM of a gamma line in the energy spectrum is given by [57]:

$$w_{\text{ENC}} = 2\sqrt{2\log 2} \frac{\epsilon}{e} \text{ENC} \quad (5.7)$$

Here, ϵ , is the average energy necessary to create an electron-hole pair in germanium. Next to the ENC noise, also statistical fluctuations in the number of created of electron-hole pairs during the charge production process influence the energy resolution. It can be expressed by [57]:

$$w_{\text{CP}} = 2\sqrt{2\log 2} \sqrt{\epsilon F E} \quad (5.8)$$

Here E denotes the absorbed energy and F the fano factor. The fano factor is a material dependant constant, that accounts for the non Poissonian nature of the process.

The third component contributing to the energy resolution is the efficiency of the charge collection of the detector and the electronic system. They are described by the empirical formula [57],

$$w_{\text{CC}} = 2\sqrt{2\log 2} c E \quad (5.9)$$

where c is a constant.

The sum of these three components leads to the formula for the energy dependant FWHM of a gamma line in the energy spectrum:

$$\text{FWHM}(E) = \sqrt{w_{\text{ENC}}^2 + w_{\text{CP}}^2 + w_{\text{CC}}^2} = 2\sqrt{2\log 2} \sqrt{\frac{\epsilon^2}{e^2} \text{ENC}^2 + FE + c^2 E^2} \quad (5.10)$$

Since the ENC noise in energy independent, is dominates for lower energies, while the others take over at higher energies.

5.1.3 CSA in LEGEND-200

To balance radiopurity and electronics performance, the CSA for LEGEND-200 consists of two parts [58]: one near the detector and one further away, as illustrated in Figure 5.2a.

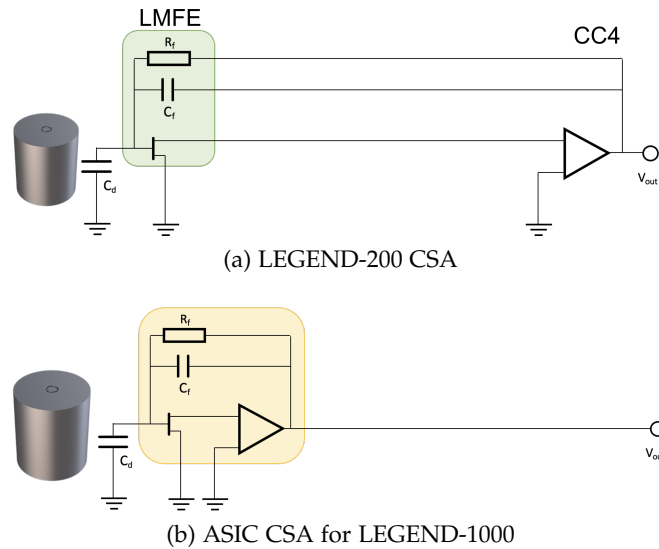


Figure 5.2: CSA versions for LEGEND. a) The CSA in LEGEND-200 is split into two parts. The LMFE close to the detector containing R_f , C_f , and the JFET, as well as the CC4 farther away containing the OpAmp. They are separated by 1.5 meters of cable. b) Sketch of an ASIC CSA approach where all components of the CSA are inside the ASIC. Sketches by Florian Henkes.

The Low Mass Front End (LMFE) is positioned close to the detector with ultra high radio purity [59]. This was achieved by constructing the entire LMFE from a Suprasil substrate with sputtered traces. The capacitance C_f is realized through stray capacitances between these traces, while the feedback resistor is a thin sputtered film of amorphous germanium (aGe).

The LMFE is followed by the second stage, the CC4, which is separated by around 1-1.5 meters of cable [60]. This separation allows the CC4 to contain less radiopure components, such as the commercial OpAmp, which can be used in a location with less stringent radiopurity requirements.

5.1.4 LUIGI ASIC

While the LMFE and CC4 approach of the LEGEND-200 offers a reasonable compromise, the design goal for LEGEND-1000 is to further improve electronic performance and radiopurity [35]. To achieve the best noise performance all components will be placed into a single chip as close as possible to the detector, as sketched in Figure 5.2b.

ASIC technology is under investigation to reach this goal, which allows the entire CSA to be merged into a single low-mass silicon chip. The chip contains Metal-oxide semiconductor field effect transistors (MOSFETs) that have similar properties as the commonly for CSA used J-FETs, but enable the integration of the complete CSA into a

single chip [61].

The LUIGI ASIC, a collaborative effort between the Technical University of Munich and the Politecnico di Milano, aims to achieve an ASIC design suitable for LEGEND which follows these specifications:

The ASIC needs to work inside LAr at cryogenic temperatures of 96K and have a low power consumption to avoid local boiling of the liquid argon. A Low-DropOut (LDO) regulator is integrated directly into the chip to guaranty stable supply voltages and avoid power supply noise, without using external filters or capacitors [62]. A dedicate line driver circuit transmits a differential Output Signal over an distance of 10 meters to the DAQ [63].

A huge challenge for ASIC technology is the implementation of a continuous RC-feedback loop with an decay time constant of $\tau \sim 100 \mu\text{s}$. The integration of an high ohmic resistor directly into the ASIC is not as simple as for an analog circuit as implemented in the LMFE.

To realise the continuous reset mechanism in the chip two different design versions are currently under investigation for the LUIGI ASIC: one with a large value external resistor and the other one with an internal reset mechanism. These two approaches will be discussed next.

LUIGI-RF ASIC

The LUIGI-RF ASIC is a version that incorporates a large value external resistor. Its circuit is sketched in Figure 5.3a. With this RC-like reset design, it behaves similarly to conventional CSA mechanisms and therefore considered the safer solution in risk evaluations. This design also has an alternative version, shown in Figure 5.3b. In this version, both the external resistor and the capacitance are located outside the ASIC.

LUIGI-IR ASIC

The LUIGI-IR ASIC operates without external components, as sketched in Figure 5.3c. It has a dedicated compensation network that implements an ICON cell to mimic the effect of a large-value resistor [64]. The integration of these components within the ASIC eliminates the need for external resistors and capacitors. Due to the internal complexity of the reset mechanism this design is regarded as the more ambitious approach.

5.2 First results of the LUIGI-RF ASIC

This section discusses the measurements with the LUIGI-RF ASIC. The main measurements were performed with the LUIGI-RF version with internal capacity. The results of the alternative version with external capacity are summarized in 5.2.3. The LUIGI-IR

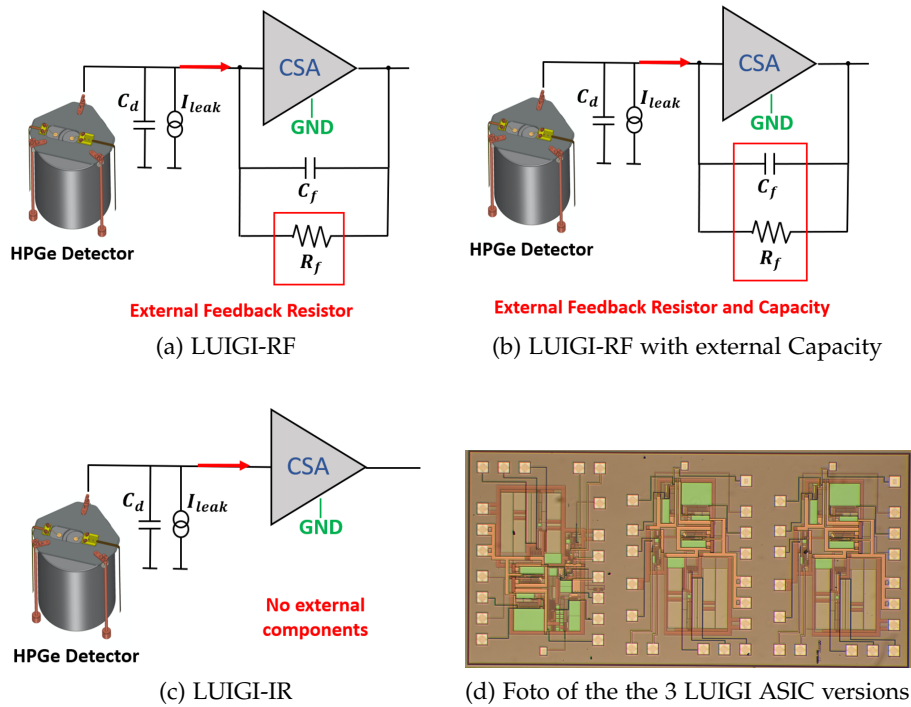


Figure 5.3: LUIGI ASIC. Figures a) -c) show the simplified circuit structures of the three different ASIC designs. Scetch by Davide Butta. Figure d) shows a photo of the 3 ASICs. Foto by Politecnico di Milano.

version was not tested in the scope of this work. The ASIC was tested in different experimental setups, that enable different testing environments. The data analysis was performed by using the JULEANA analysis framework [40].

5.2.1 Bench tests with the LUIGI-RF ASIC

The initial tests of the ASIC were conducted as quick bench tests. During these tests, the ASIC was mounted to a PCB (printed circuit board) inside a copper box. Through holes in the copper box, cables were routed for powering the chip, connecting a pulse generator to create signals, and for the readout that fed into an oscilloscope acquiring the data. The box was submerged into a bath of liquid nitrogen to cool down the ASIC to cryogenic temperatures, simulating the conditions faced during operation in LEGEND.

Ringng Waveforms

During one of the first bench test the ASIC was mounted on a PCB submerged in a copper box within liquid nitrogen. A pulser (KEYSIGHT 33500B Series) was used to

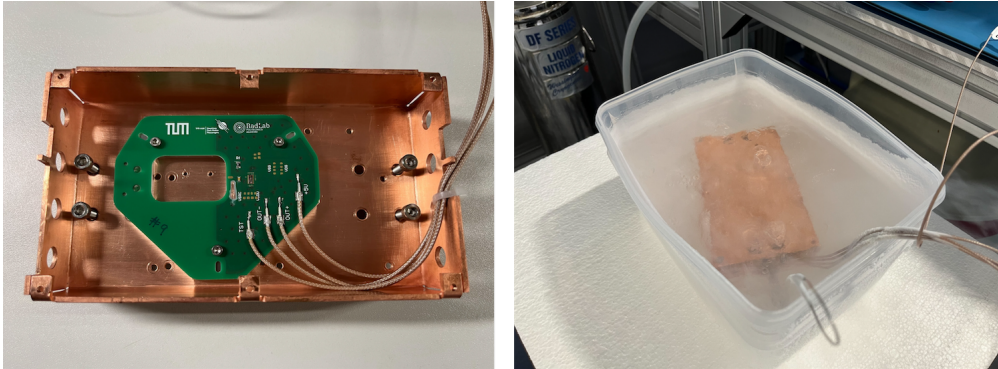


Figure 5.4: Bench test setup. The left picture shows the ASIC mounted on a PCB inside a copper box. It is connected through holes to a pulser and an oscilloscope. To cool the ASIC to cryogenic temperatures as experienced during operation in LEGEND, the copper box is lowered into a bath of liquid nitrogen. Photos by Michael Willers.

generate square pulses with a height of 1.2 V and varying edge times. The output signal of the ASIC was recorded using an oscilloscope (Tektronix MSO44). Figure 5.5a displays two examples of these waveforms. Notably, oscillations are present near the rising edge of the waveforms, particularly for fast pulser edge times. This ringing is problematic because the signal of the rising edge is critical for PSD. Additional features introduced by the ringing can obscure the distinction between signal and background events, thereby reducing the efficiency of analysis cuts. To address this issue, a bypass capacitor $C_{bypass} = 4.7 \mu\text{f}$ was added to the supply voltage. Consequently, the waveforms show the expected behavior, without oscillations, as shown in Figure 5.5b.

Noise Performance

As explained in section 5.1.2 Electronic noise consists of unwanted disturbances in the signal, leading to a worsening in energy resolution. Because of this noise should be minimized.

For the noise performance measurement a noise sweep was performed. During this measurement different filter shaping times are used when applying a filter and the ENC noise is measured. With this measurement, the optimal shaping time that minimizes the ENC noise can be measured. A waveform generator was used to produce a signal that was fed into a shaper (ORTEC 672) and then a MCA (ORTEC 927). This setup allows for analog signal processing which ensures that the measured noise originates purely from the ASIC and not from the electronic devices that would digitize the signal.

The ENC noise is measured in terms of the baseline voltage and subsequently converted into Energy. The results of this measurement are shown in Figure 5.6a. It displays the measured electronic noise for different shaping times and various external resistors R_f . A high feedback resistance reduces the parallel ENC noise component as described in

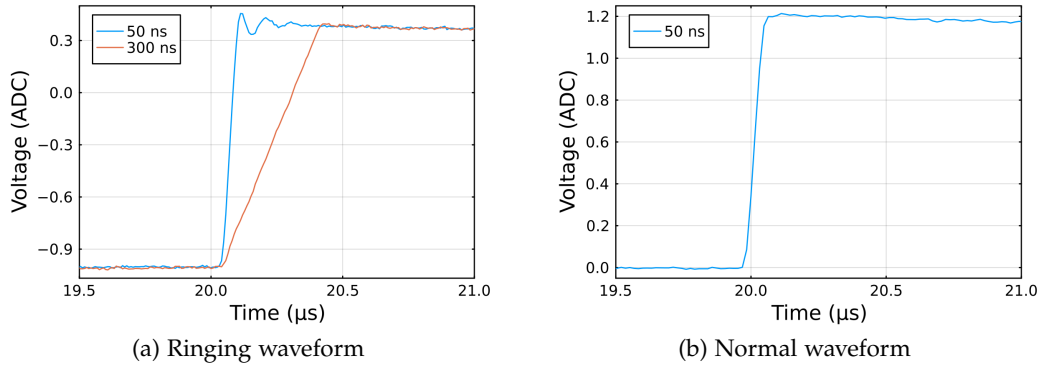


Figure 5.5: Waveforms created by a pulser recorded during initial ASIC bench tests at cryogenic temperatures. (a) without and (b) with bypass capacitor connected to the supply voltage.

equation 5.3. Because of this the lowest electronic noise levels are achieved with a high R_f . While the reduction of noise improves the energy resolution, R_f can not be chosen arbitrarily large, as it increases the decay constant as described in equation 5.1. This increase in signal decay time would lead to an increase of pile-up events, where a signal is produced in the decay tail of an previous event. This leads to an incorrect energy estimation and therefore should not occur. Because of this an compromise between noise reduction and signal decay time needs to be found. Typically τ is chosen to be around $100\mu\text{s}$, which allows for R_f to be a few hundred $\text{M}\Omega$ since $C_f = 400\text{ fF}$.

The obtained ENC values, that were shown in figure 5.6a were fit with the ENC formula of equation 5.2. The fit for measurement with $R_f = 1\text{ G}\Omega$ is shown in 5.6b, as it had the lowest ENC noise. For shaping times of $6.6\mu\text{s}$ the lowest ENC noise level of 496 eV was achieved. Figure 5.6a also shows the noise components of 5.2. For shaping times below $5\mu\text{s}$ the series noise is dominating, for higher shaping times the parallel noise becomes dominant.

5.2.2 Detector Measurements

To test the energy linearity and resolution, the ASIC was operated with a HPGe Germanium detector in the CUBE³ setup [43]. This experiment setup is used for measurements at cryogenic temperatures inside a vacuum. The cryostat has a lock door, allowing easy access. When closed, a vacuum pump (Pfeiffer HiCUBE) creates a vacuum of approximately 10^{-7} mbar. During measurements this pump is turned off, to avoid noise procured by it. The cryogenic temperatures are achieved by thermally coupling the detector, with a cold finger situated in a dewar filled with liquid nitrogen. Data is recorded through a feedthrough flange by a DAQ system of choice. A sketch of the setup can be seen in Figure 5.7a.

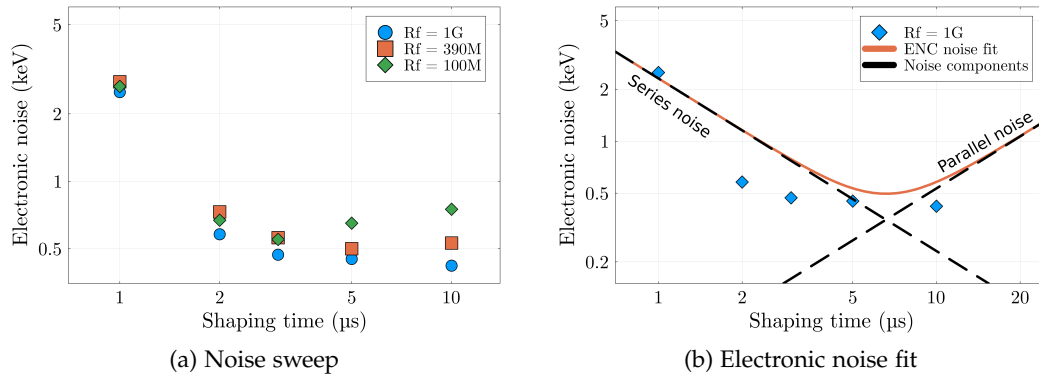


Figure 5.6: ENC noise measurement. Figure a) shows the measured ENC noise for shaping times and external resistors. Figure b) shows a fit of the ENC noise curve. The parallel and series noise components are highlighted. For a shaping time of $6.6\mu\text{s}$ the ENC noise is minimized to 496 keV .

To estimate the energy linearity and resolution the ASIC was operated with the HPGe Germanium detector inside the CUBE³ setup. The detector used for the measurement is an BEGe detector with a height of 28 mm, a diameter of 70 mm and it weighs 350g. A ^{228}Th source was placed next to the experiment setup to produce signals by high energetic gammas in the germanium detector. To the Germanium detector a high voltage was applied, so it was fully biased. Data was taken two with different types of DAQ, one using a Spectroscopy amplifier (ORTEC 672) and an MCA (ORTEC 927), the other by using a buffer amplifier and Flashcam to digitize the signals.

For the estimation of the energy resolution the measurements with the MCA were used. Normally Flashcam would be the DAQ system of choice, since it mimics best the conditions in LEGEND, but it requires a buffer amplifier. This additional component can result in a worse energy linearity, therefore the thorium spectrum for the energy linearity measurement was obtained using a MCA.

During the measurement $1.1 \cdot 10^6$ events were recorded. A gaussian shaper with a shaping time of $\tau = 6\ \mu\text{s}$ was used to capture the spectrum with the MCA. The spectrum is shown in Figure 5.8a. Some peaks in the spectrum were fitted to obtain their positions. The fit for one of the peaks (the ^{208}Tl FEP) is shown in Figure 5.8b. The peaks were fitted with the JULEANA gamma peak fit shape which is explained in A. These results of the fits are then used to calculate the linearity. The peaks used during the analysis are listed in Table 5.1.

With the fit of the peaks, their position was obtained. Since the literature values of the gamma lines peak positions are well known, they can be compared to their measured values. Figure 5.9 shows the evaluated peak positions in ADC compared to the literature values for the peaks in keV. A linear function is fitted through the data

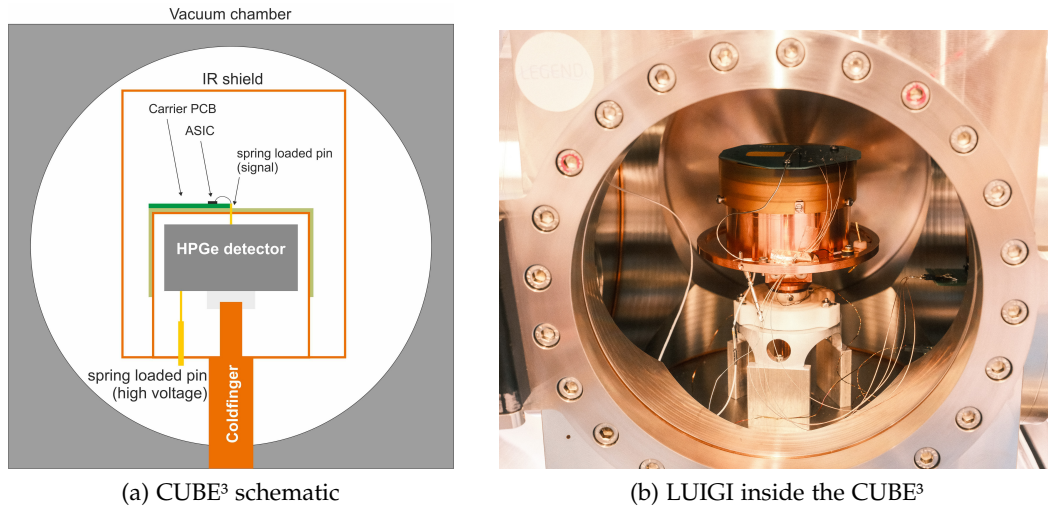


Figure 5.7: CUBE³ test stand. (a) Schematic of the CUBE³ testing setup. During the measurements the ASIC was mounted on a PCB and connected to a HPGe detector for thermal coupling to the cold finger. Schematic by Michael Willers (b) Picture of the LUIGI ASIC together with a Germanium detector inside the CUBE³ testing setup. Photo by Michael Willers

Isotope	Energy (keV)	Intensity (%)	Isotope	Energy (keV)	Intensity (%)
²⁰⁸ Tl	583.187(2)	85.0(3)	²⁰⁸ Tl	1592.511(10)	DEP
²¹² Bi	727.330(9)	6.67(9)	²⁰⁸ Tl	2103.511(10)	SEP
²⁰⁸ Tl	860.557(4)	12.5(1)	²⁰⁸ Tl	2614.511(10)	99.754(4)

Table 5.1: Isotopes, their energy levels, and intensities of the used gamma lines for the analysis. Data from [44]

points. The residuals from the data to the fitted function are shown at the bottom, indicating that the residuals are below 0.004%, demonstrating very good linearity over the energy range of the peaks.

For the measurement of the energy resolution the ASIC was also measured in the CUBE³ setup at cryogenic temperatures. Again a ²²⁸Th source was placed next to the setup to produce signals in the germanium detector. The difference compared to the energy linearity measurement is, that a FlashCam together with an buffer amplifier was used as an DAQ system. With this DAQ the measurement data was digitized.

The extraction of the energy from the waveforms was performed in julia using the JULENA analysis framework [40]. During the DSP a noise sweep was performed to obtain the ideal shaping time. Additionally different filter types were tested, the best resolution was obtained by applying a trapezoidal filter for energy extraction.

Again the peaks shown in table 5.1 were fitted. The energy resolution is then measured

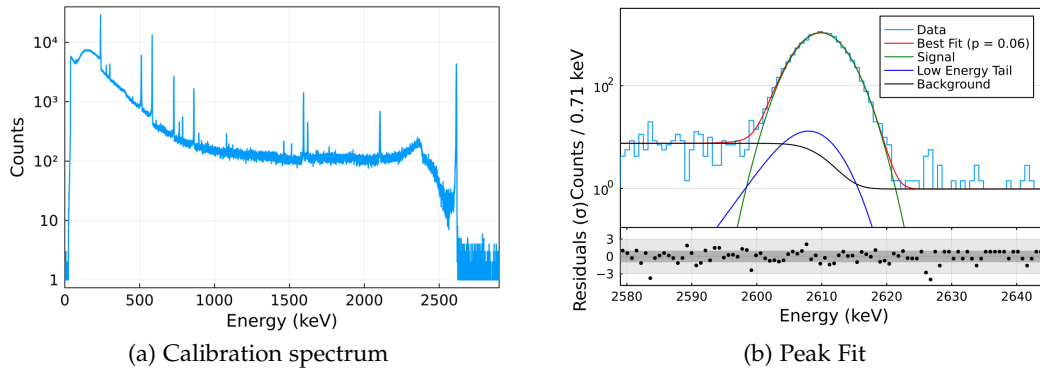


Figure 5.8: a) Thorium spectrum taken with a MCA and a Gaussian shaping using the LUIGI-RF ASIC as readout electronics. b) Fit of one of the peaks. The position and FWHM of the peaks are used to estimate energy linearity and resolution. Plot style based on [65].

by analyzing the full width at half maximum (FWHM) of several peaks. A square root equation is used to fit the data.

The FWHM fit obtained during the first measurement of the ASIC inside the CUBE³ setup is shown in Figure 5.10a. For this fit, the SEP and DEP are excluded due to their larger FWHM caused by Doppler broadening. The green line indicates the energy resolution at $Q_{\beta\beta}$. The energy resolution observed was three times worse than anticipated, as the ASIC achieved a resolution of 7.20 keV at $Q_{\beta\beta}$.

The cause of this poor energy resolution was identified as the low-dropout regulator (LDO), which was not functioning as expected. The LDO is intended to mitigate small voltage fluctuations and maintain a stable input voltage for the chip. It has an input voltage of 5.0V and should output a constant voltage of 3.8V. However, the LDO's malfunctioning drastically worsens the energy resolution. To resolve this issue, the input voltage was reduced to 3.8V, effectively bypassing the LDO and directly supplying 3.8V to the rest of the chip. This adjustment significantly improved the energy resolution to 2.64 keV at $Q_{\beta\beta}$, as shown in Figure 5.10b.

The effect of reducing the voltage can also be observed in a periodogram. For this analysis, the ASIC was operated for different input voltages V_{DD} together with the HPGe detector. First a thorium source was next to detector and the spectrum was used to calibrate the detector. Then the Flashcam system was configured to trigger only on baseline events. The baseline events were then converted into a periodogram. The results are shown in Figure 5.11. At $V_{DD} = 5.0V$, the power, which is related to noise at a given frequency, is highest. Reducing V_{DD} improves performance, with the most significant improvement observed at $V_{DD} = 3.8V$, where the LDO is completely bypassed, drastically lowering the power.

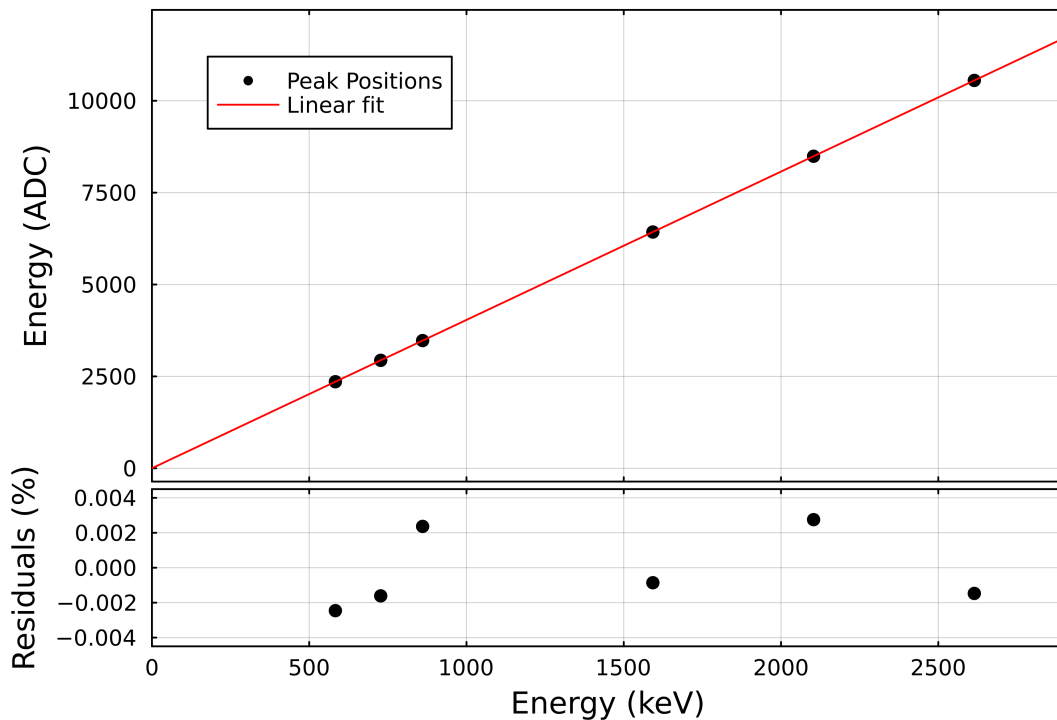


Figure 5.9: Energy linearity during testing of the LUIGI-RF ASIC. The evaluated peak positions in ADC are compared to literature values for the peaks in keV. A linear function was used to fit the data. Residuals are shown at the bottom.

Additionally there was a second effect lowering the energy resolution. Analysing the waveform shape, it was observed that the waveforms still showed an exponential tail after a standard pole-zero correction. Figure 5.12 shows superpulses created by averaging 100 waveforms. The figure indicates that the pole-zero corrected waveform shows multiple poles. This implies that the ASIC produces waveforms with more than one decay time constants. To achieve a flat tail in these waveforms, a double pole-zero correction is necessary, as illustrated by the green waveform in Figure 5.12.

The second decay constant can be problematic for data analysis if not appropriately treated. It can lead to a case where the energy of the event is not correctly reconstructed and therefore result in degraded detector performance. Figure 5.13 shows the energy resolution after a double pole-zero correction was applied.

The energy resolution is slightly better for the double pole-zero corrected version, than for the single-pole zero corrected version shown in 5.10b. This highlights the adverse impact of the second decay constant if not properly addressed. Furthermore, the second decay can negatively affect the performance of the LQ cut, where it is crucial for the waveform tail to be flat to prevent additional influences on the areas used in LQ

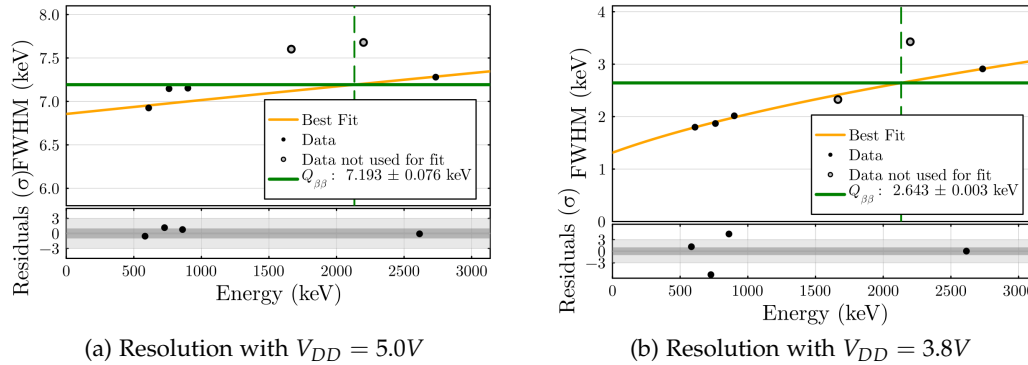


Figure 5.10: Energy resolution of the LUIGI-RF ASIC. The FWHM of the peaks in the thorium calibration measurement are fitted by a square root function to estimate the energy resolution at $Q_{\beta\beta}$. Different supply voltages were used during the measurements, in Figure (a) $V_{DD} = 5.0V$ and (b) $V_{DD} = 3.8V$. Plot style based on [65].

parameter extraction (see section 4).

With this improvements the best energy resolution was measured to be 2.44 keV. This meets the expectations for the energy resolution. As describe in equation 5.10, the ENC noise is the main driving factor at low energies in the FWHM curve. Its contribution can therefore be estimated by analyzing by the y-intercept of the FWHM fit function. The ENC noise for the detector measurement is therefore 1.4 keV. It is higher than during the noise sweep, because during that measurement the detector was not connected. The detector capacitance increases the total capacitance and therefore the $ENC_{1/f}$ and ENC_s^2 noise components.

5.2.3 Results of the LUIGI-RF ASIC version with an external Capacity

The LUIGI-RF ASIC has two different specifications, one main version where the capacity is situated inside of the ASIC, and an alternative version, where a external capacity could be used. In general it is favorable to put all components inside of the ASIC to improve overall performance, since additional outside part can produce additional backgrounds and require additional handling and installation. While the main version of the LUIGI-RF ASIC was therefore the preferred solution, the alternative version was used as an backup, and allowed for more flexibility during testing by the possibility to also change the value of the capacity.

While the two version are quite similar, differences are visible when waveforms of the alternative LUIGI-RF ASIC, shown in Figure 5.2.3 are compared to the waveforms of the main version shown in Figure 5.12. While the waveform of the main ASIC version is mostly flat, the alternative version shows features within its tail. This is an unwanted feature and shows that this ASIC version is not behaving as predicted.

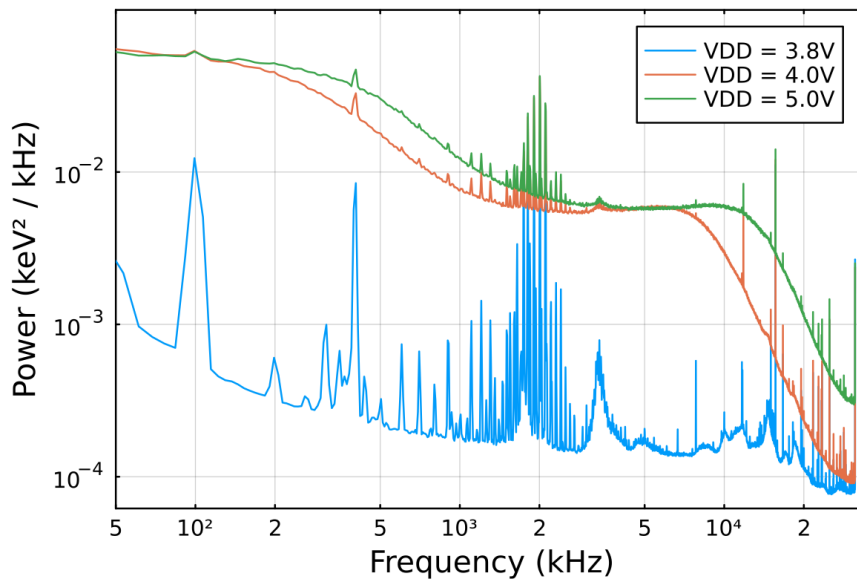


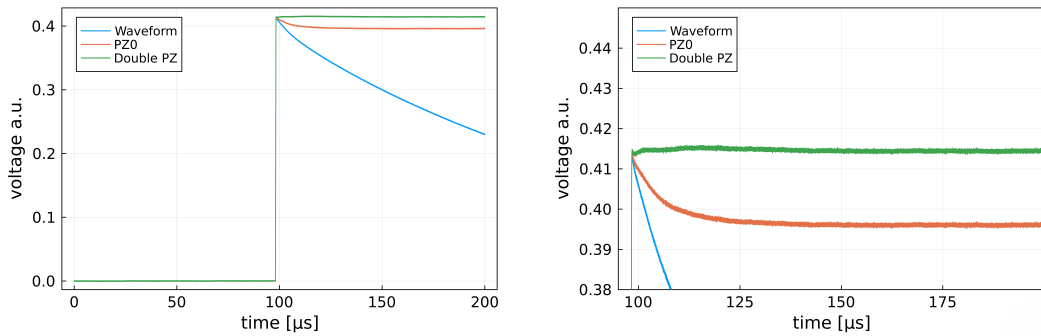
Figure 5.11: Periodogram of baseline events. The LUIGI ASIC was operated together with a HPGe detector at different V_{DD} settings. For $V_{DD} = 3.8V$, where LDO is effectively bypassed, the Power becomes the lowest.

5.3 Conclusion and changes for the second version of the LUIGI ASIC

The LUIGI ASIC demonstrated during the initial measurements its potential as a CSA for the LEGEND-1000 project. The LUIGI-RF version showed meet the expectations for the electronic noise, energy linearity, and energy resolution. With these first promising results a second iteration of the ASIC will be developed, that tackles the issues that were observed.

As discussed, the LDO appears to not work properly and worsens the energy resolution. In addition, it was observed that the tail of the waveform can not be described by one single decay constant. While this can be fixed during analysis with a double pole-zero correction, ideally the ASIC produces waveforms with a single decay time constant.

Another problem lies in handling the ASIC when it comes to Electro Static Discharges (ESD). In several test the ASIC was submerged together with an HPGe detector in liquid nitrogen. This would mimic the conditions experienced in LEGEND more precisely than the CUBE³ setup, where ASIC and detector are in a vacuum. The detector and ASIC are first assembled in a nitrogen filled glovebox and from there lowered into a dewar filled with liquid nitrogen. However, after the installation process the ASIC always stopped producing signals. The most likely reason for this are ESD in the dry glovebox atmosphere. This poses a challenge for LEGEND-1000 where the detectors



(a) Superpulsed waveforms without and with different pole-zero corrections (b) Zoomed on the tail of the waveforms of Figure a)

Figure 5.12: 1000 waveforms averaged to created superpulses. The blue waveform is the original superpuls, the orange one after a pole zero-correction, and the green one after a double pole-zero correction.

electronics will also be assembled ins such conditions. To mitigate this risk, protective diodes will be added be added to the ASIC.

Furthermore, the secondary LUIGI-IR ASIC with the internal reset mechanism needs to be investigated. First promising tests were conduct by a group from PoLiMi of the ASIC alone, but the ASIC will also be tested together with an HPGE detector in further experiments at TUM.

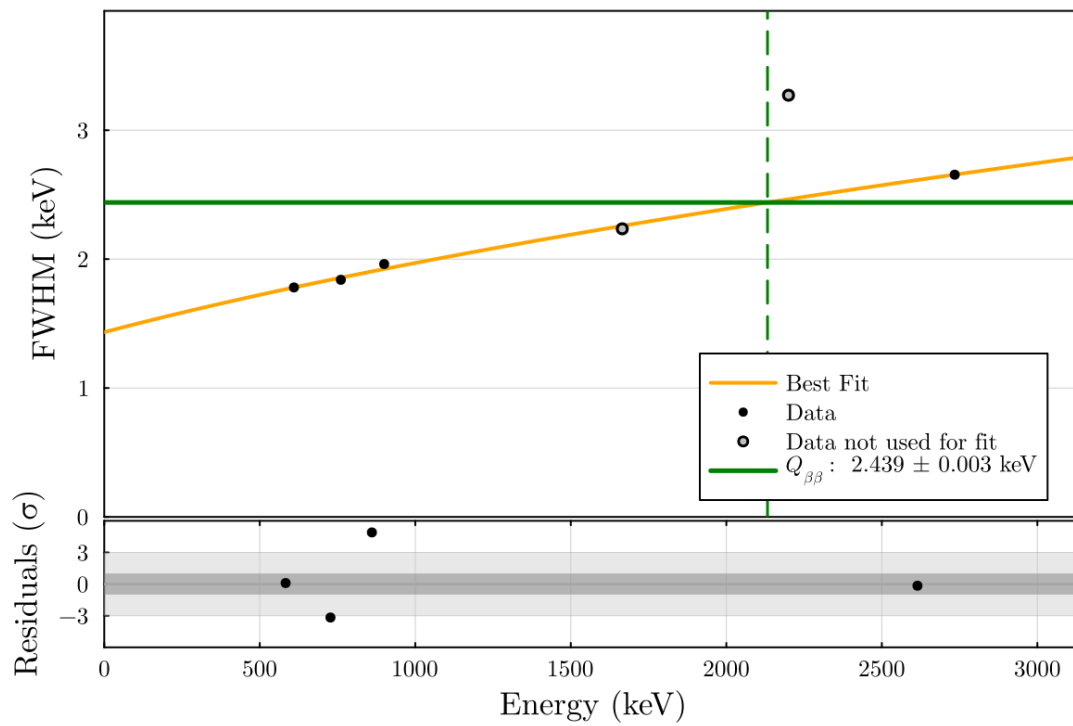
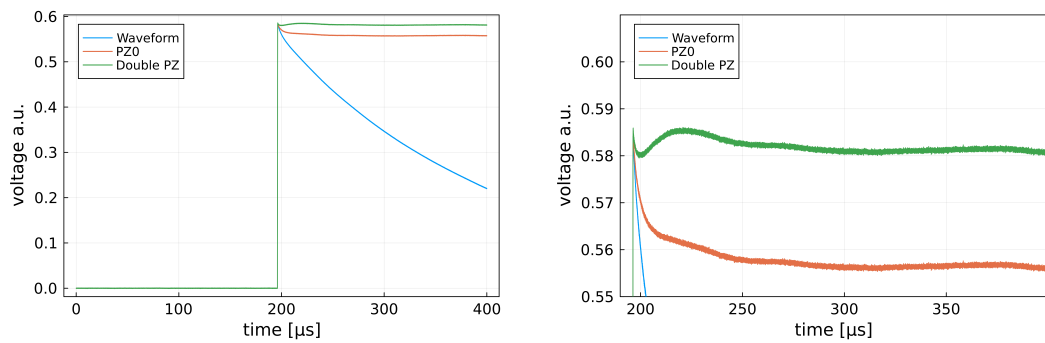


Figure 5.13: Energy resolution of the LUIGI-RF ASIC as a function of energy, with $V_{DD} = 3.8$ V and a double pole-zero correction. The peak FWHM were with a square root fit to estimate the energy resolution at $Q_{\beta\beta}$, which is indicated by the green line. Plot style based on [65].



(a) Superpulsed waveforms without and with different pole-zero corrections (b) Zoomed on the tail of the waveforms of Figure a)

Figure 5.14: Measurement of the alternative LUIGI-RF version. 1000 waveforms averaged to created superpulses. The blue waveform is the original superpuls, the orange one after a pole zero-correction, and the green one after a double pole-zero correction.

Chapter 6

Summary and outlook

The LEGEND experiment is one of the most promising experiments searching for $0\nu\beta\beta$. Its build upon the knowledge of GERDA and MAJORANA to set the world leading limit on the ^{76}Ge $0\nu\beta\beta$ decay. The final phase LEGEND-1000 will operate 1000 kg of HPGe detectors highly enriched with the isotope ^{76}Ge over 10 years to reach a signal discovery sensitivity on the decay half-life of $T_{1/2}^{0\nu} > 10^{28}\text{yr}$. To reach this ambitious goal a background index $\text{BI} < 10^{-5}\text{cts}/(\text{keV} \cdot \text{kg} \cdot \text{yr})$ is envisioned. This necessitates the development of the best methods possible in suppressing background. In this thesis two of these methods are investigated, namely the late charge (LQ) cut and the LUIGI ASIC.

LQ cut

An important part of background reduction is achieved during the LEGEND data analysis. With the powerful tool of pulse shape discrimination background events can be identified and rejected. An important parameter for this analysis is the LQ classifier. The parameter is sensitive to deviations in the top part of the the waveforms rising edge, which mainly helps to identify surface events, where a particle deposits its energy close to the detector surface. Especially p-type point contact (PCC) detectors are very susceptible to those kind of events due to their large passivated surface.

In this work a the first version of the LQ cut was implemented into the secondary LEGEND software stack JULEANA (Julia LEGEND analysis). This includes the extraction the raw LQ parameter, an energy and drift time correction to get the LQ classifier, as well as the estimation of the final cut value. The LQ cut was applied to the LEGEND-200 calibration runs of period 3. The results show that with the use of the LQ classifier background events run can be identified and rejected.

With this first successfully implementation of the LQ cut with calibration data, it now needs to be tested on physics data to evaluate the overall effectiveness of the cut. It also needs to be compared to other pulse shape discrimination cuts and checked if its

able to cut events missed by those and therefore benefits the analysis. Additionally the results of the JULEANA LQ implementation should be compared to those of the primary software stack to crosscheck and verify the results.

LUIGI ASIC

To improve upon the electronics used in LEGEND-200, a novel approach based on ASIC technology is investigated. It would allow to fit the whole CSA into a single low-mass silicon chip. The LUIGI ASIC presents two different solutions to this challenge. The LUIGI-RF version incorporates a large value external resistor, while the LUIGI-IR ASIC implements a transistor with dedicated compensation network that mimics the effect of a large value resistor without using any external components.

In this work, the LUIGI-RF version was evaluated. During bench test the electronic noise of the ASIC was measured to be 496 eV, fulfilling the design goal. A measurement with a HPGe detector was performed to verify energy linearity and measure the energy resolution. The ASIC demonstrated good energy linearity with residuals below 0.004%, and met the expectations for the energy resolution with an FWHM of 2.44 keV at $Q_{\beta\beta}$. The alternative version of the LUIGI-RF ASIC with an external capacity deviated from the expected waveform, and is therefore less favored compared to the version with the internal capacity.

A secondary iteration of the LUIGI can build upon the promising results and tackle the problems of the non functioning LDO, ESD, and the additional decay time components, observed during the testing. The LUIGI-IR version, which was not tested in the scope of this work, also needs to be tested to explore its possibility as the CSA for LEGEND-1000.

Appendix A

JULEANA gamma peak fit shape

The gamma peakshape function implemented in the LegendSpecFits JULEANA package and used for the peak shape fitting consists of an gaussian for the main gamma peak, and exponential modified gaussian for a low energy tail, a step gaussian function for the compton continuum and a constant for background. It is defined as follows:

$$\begin{aligned}\gamma_{\text{peakshape}}(x, \mu, \sigma, n, A, f, w, b) = & n [(1 - f) \cdot \text{Gaussian}(x, \mu, \sigma) \\ & + f \cdot \text{ExponentialGaussian}(-x, -\mu, \sigma, w \cdot \mu)] \quad (\text{A.1}) \\ & + A \cdot \text{StepGaussian}(-x, -\mu, \sigma) + b\end{aligned}$$

where:

$$\text{Gaussian}(x, \mu, \sigma) = \frac{1}{\sigma\sqrt{2\pi}} \exp\left(-\frac{(x - \mu)^2}{2\sigma^2}\right) \quad (\text{A.2})$$

$$\text{StepGaussian}(x, \mu, \sigma) = \frac{1}{2} \text{erfc}\left(\frac{\mu - x}{\sigma\sqrt{2}}\right) \quad (\text{A.3})$$

$$\text{ExponentialGaussian}(x, \mu, \sigma, \theta) = \text{Gaussian}(x, \mu, \sigma) \times \frac{\sigma}{\theta} \sqrt{\frac{\pi}{2}} \text{erfcx}\left(\frac{\sigma}{\theta\sqrt{2}} - \frac{x - \mu}{\sigma\sqrt{2}}\right) \quad (\text{A.4})$$

Bibliography

- [1] Wolfgang Pauli. “Pauli letter collection: letter to Lise Meitner”. Typed copy. URL: <https://cds.cern.ch/record/83282>.
- [2] J. Chadwick. “Possible Existence of a Neutron”. In: *Nature* 129 (1932), p. 312. DOI: 10.1038/129312a0. URL: <https://doi.org/10.1038/129312a0>.
- [3] J. Chadwick. “The existence of a neutron”. In: *Proceedings of the Royal Society of London. Series A, Containing Papers of a Mathematical and Physical Character* 136 (830 1932), pp. 692–708. DOI: 10.1098/rspa.1932.0112.
- [4] C. L. Cowan et al. “Detection of the Free Neutrino: a Confirmation”. In: *Science* 124.3212 (1956), pp. 103–104. DOI: 10.1126/science.124.3212.103.
- [5] John N. Bahcall and Raymond Davis. “Solar Neutrinos: A Scientific Puzzle”. In: *Science* 191.4224 (1976), pp. 264–267. DOI: 10.1126/science.191.4224.264.
- [6] Raymond Davis, Don S. Harmer, and Kenneth C. Hoffman. “Search for Neutrinos from the Sun”. In: *Phys. Rev. Lett.* 20 (21 May 1968), pp. 1205–1209. DOI: 10.1103/PhysRevLett.20.1205.
- [7] Q. R. Ahmad et al. “Direct Evidence for Neutrino Flavor Transformation from Neutral-Current Interactions in the Sudbury Neutrino Observatory”. In: *Phys. Rev. Lett.* 89 (1 June 2002), p. 011301. DOI: 10.1103/PhysRevLett.89.011301.
- [8] Y. Fukuda et al. “Evidence for Oscillation of Atmospheric Neutrinos”. In: *Phys. Rev. Lett.* 81 (8 Aug. 1998), pp. 1562–1567. DOI: 10.1103/PhysRevLett.81.1562.
- [9] Ziro Maki, Masami Nakagawa, and Shoichi Sakata. “Remarks on the Unified Model of Elementary Particles”. In: *Progress of Theoretical Physics* 28.5 (Nov. 1962), pp. 870–880.
- [10] A. Yu. Smirnov. “The MSW effect and solar neutrinos”. In: *10th International Workshop on Neutrino Telescopes*. arXiv:hep-ph/0305106. May 2003, pp. 23–43.
- [11] Frank Edzards. “Characterization of Point Contact Germanium Detectors and Development of Signal Readout Electronics for LEGEND”. PhD thesis. TU München Munich, 2021.
- [12] M. Goeppert-Mayer. “Double Beta-Disintegration”. In: *Phys. Rev.* 48 (6 Sept. 1935), pp. 512–516. DOI: 10.1103/PhysRev.48.512.
- [13] Vladimir I. Tretyak and Yuri G. Zdesenko. “Tables of Double Beta Decay Data—An Update”. In: *Atomic Data and Nuclear Data Tables* 80.1 (2002), pp. 83–116. ISSN: 0092-640X. DOI: <https://doi.org/10.1006/adnd.2001.0873>.

- [14] W. H. Furry. "On Transition Probabilities in Double Beta-Disintegration". In: *Phys. Rev.* 56 (12 Dec. 1939), pp. 1184–1193. DOI: 10.1103/PhysRev.56.1184.
- [15] J. Schechter and J. W. F. Valle. "Neutrinoless double- β decay in SU(2) \times U(1) theories". In: *Phys. Rev. D* 25 (11 June 1982), pp. 2951–2954. DOI: 10.1103/PhysRevD.25.2951.
- [16] P. A. Zyla et al. "Review of Particle Physics". In: *Progress of Theoretical and Experimental Physics* 8 (2020). 2021 update, p. 083C01.
- [17] A. Gando et al. "Search for Majorana Neutrinos near the Inverted Mass Hierarchy Region with KamLAND-Zen". In: *Physical Review Letters* 117.8 (2016). Addendum: *Phys. Rev. Lett.* 117, 109903 (2016), p. 082503. arXiv: 1605.02889 [hep-ex].
- [18] Matteo Agostini et al. "Toward the discovery of matter creation with neutrinoless double beta decay". In: *Reviews of Modern Physics* 95.2 (May 2023). ISSN: 1539-0756. DOI: 10.1103/revmodphys.95.025002.
- [19] Glenn F. Knoll. *Radiation Detection and Measurement*. 4th. Wiley, 2010. ISBN: 9780470131480. URL: <https://www.wiley.com/en-us/Radiation+Detection+and+Measurement%2C+4th+Edition-p-9780470131480>.
- [20] F. E. Emery and T. A. Rabson. "Average Energy Expended Per Ionized Electron-Hole Pair in Silicon and Germanium as a Function of Temperature". In: *Phys. Rev.* 140 (6A Dec. 1965), A2089–A2093. DOI: 10.1103/PhysRev.140.A2089.
- [21] R. K. Schaevitz et al. "Indirect absorption in germanium quantum wells". In: *AIP Advances* 1.3 (Sept. 2011), p. 032164. ISSN: 2158-3226. DOI: 10.1063/1.3646149.
- [22] Y.P. Varshni. "Temperature dependence of the energy gap in semiconductors". In: *Physica* 34.1 (1967), pp. 149–154. ISSN: 0031-8914. DOI: [https://doi.org/10.1016/0031-8914\(67\)90062-6](https://doi.org/10.1016/0031-8914(67)90062-6).
- [23] W. Shockley. "Currents to Conductors Induced by a Moving Point Charge". In: *Journal of Applied Physics* 9.10 (Oct. 1938), pp. 635–636. ISSN: 0021-8979. DOI: 10.1063/1.1710367.
- [24] S. Ramo. "Currents Induced by Electron Motion". In: *Proceedings of the IRE* 27.9 (1939), pp. 584–585. DOI: 10.1109/JRPROC.1939.228757.
- [25] A. Balysh et al. "The Heidelberg-Moscow double beta decay experiment with enriched ^{76}Ge . First results". In: *Physics Letters B* 283.1 (1992), pp. 32–36. ISSN: 0370-2693. DOI: [https://doi.org/10.1016/0370-2693\(92\)91421-5](https://doi.org/10.1016/0370-2693(92)91421-5).
- [26] C. E. Aalseth et al. "IGEX ^{76}Ge neutrinoless double-beta decay experiment: Prospects for next generation experiments". In: *Phys. Rev. D* 65 (9 May 2002), p. 092007. DOI: 10.1103/PhysRevD.65.092007.
- [27] P.N. Luke et al. "Low capacitance large volume shaped-field germanium detector". In: *IEEE Transactions on Nuclear Science* 36.1 (1989), pp. 926–930. DOI: 10.1109/23.34577.
- [28] N. Abgrall et al. "The MAJORANA DEMONSTRATOR Neutrinoless Double-Beta Decay Experiment". In: *Advances in High Energy Physics* 2014.1 (), p. 365432. DOI: <https://doi.org/10.1155/2014/365432>.
- [29] M Agostini et al. "Signal modeling of high-purity Ge detectors with a small read-out electrode and application to neutrinoless double beta decay search in

- Ge-76". In: *Journal of Instrumentation* 6.03 (Mar. 2011), P03005. DOI: 10.1088/1748-0221/6/03/P03005.
- [30] Tommaso Comellato, Matteo Agostini, and Stefan Schönert. "Charge-carrier collective motion in germanium detectors for $\beta\beta$ -decay searches". In: *European Physical Journal C* 81.76 (2021). DOI: 10.1140/epjc/s10052-021-08889-0.
- [31] Mark Thomson. *Modern Particle Physics*. Cambridge University Press, 2013.
- [32] M. Agostini et al. "Final Results of GERDA on the Search for Neutrinoless Double beta Decay". In: *Physical Review Letters* 125.25 (Dec. 2020). ISSN: 1079-7114. DOI: 10.1103/physrevlett.125.252502.
- [33] I. J. Arnquist et al. "Final Result of the Majorana Demonstrator's Search for Neutrinoless Double- β Decay in ^{76}Ge ". In: *Phys. Rev. Lett.* 130 (6 Feb. 2023), p. 062501. DOI: 10.1103/PhysRevLett.130.062501.
- [34] Matteo Agostini, Giovanni Benato, and Jason A. Detwiler. "Discovery probability of next-generation neutrinoless double- β decay experiments". In: *Phys. Rev. D* 96 (5 Sept. 2017), p. 053001. DOI: 10.1103/PhysRevD.96.053001.
- [35] LEGEND Collaboration et al. *LEGEND-1000 Preconceptual Design Report*. 2021. arXiv: 2107.11462.
- [36] F Edzards and for the LEGEND Collaboration. "The Future of Neutrinoless Double Beta Decay Searches with Germanium Detectors". In: *Journal of Physics: Conference Series* 1690.1 (Dec. 2020), p. 012180. DOI: 10.1088/1742-6596/1690/1/012180.
- [37] K.-H. Ackermann et al. "The GERDA experiment for the search of $0\nu\beta\beta$ decay in ^{76}Ge ". In: *European Physical Journal C* 73.2330 (2013). DOI: 10.1140/epjc/s10052-013-2330-0.
- [38] Brady Bos on behalf of the LEGEND collaboration. *LEGEND-200 Data Acquisition, Monitoring and Calibration*. Poster presented at the XVIII International Conference on Topics in Astroparticle and Underground Physics (TAUP 2023), September 18-22, 2023. 2023. URL: <https://indico.cern.ch/event/1199289/contributions/5447379/>.
- [39] Matteo Agostini et al. *pygama*. Version v2.0.1. May 2024. DOI: 10.5281/zenodo.11403692.
- [40] *Juleana.jl - A meta-package for the Julia software stack of the LEGEND experiment*. URL: <https://github.com/legend-exp/Juleana.jl>.
- [41] P. Födisch et al. "Digital high-pass filter deconvolution by means of an infinite impulse response filter". In: *Nuclear Instruments and Methods in Physics Research Section A: Accelerators, Spectrometers, Detectors and Associated Equipment* 830 (2016), pp. 484–496. ISSN: 0168-9002. DOI: <https://doi.org/10.1016/j.nima.2016.06.019>.
- [42] A. Domula et al. "Pulse shape discrimination performance of inverted coaxial Ge detectors". In: *Nuclear Instruments and Methods in Physics Research Section A: Accelerators, Spectrometers, Detectors and Associated Equipment* 891 (2018), pp. 106–110. ISSN: 0168-9002. DOI: <https://doi.org/10.1016/j.nima.2018.02.056>.

- [43] F. Edzards et al. "Investigation of ASIC-based signal readout electronics for LEGEND-1000". In: *Journal of Instrumentation* 15.09 (Sept. 2020), P09022. DOI: 10.1088/1748-0221/15/09/P09022.
- [44] Brookhaven National Laboratory National Nuclear Data Center. *Nudat 2.8*. Accessed on 07/24/2024. 2022. URL: <https://www.nndc.bnl.gov/nudat3/chartNuc.jsp>.
- [45] Frank Edzards et al. "Surface Characterization of P-Type Point Contact Germanium Detectors". In: *Particles* 4.4 (Oct. 2021), pp. 489–511. ISSN: 2571-712X. DOI: 10.3390/particles4040036.
- [46] E Aguayo et al. "Characteristics of signals originating near the lithium-diffused N+ contact of high purity germanium p-type point contact detectors". In: *Nuclear Instruments and Methods in Physics Research Section A: Accelerators, Spectrometers, Detectors and Associated Equipment* 701 (2013), pp. 176–185.
- [47] R.J. Cooper et al. "Effect of a surface channel on the performance of a P-type Point Contact HPGe detector". In: *Nuclear Instruments and Methods in Physics Research Section A: Accelerators, Spectrometers, Detectors and Associated Equipment* 680 (2012), pp. 48–55. ISSN: 0168-9002. DOI: <https://doi.org/10.1016/j.nima.2012.04.005>.
- [48] Steven E. Boggs. "Modeling charge cloud dynamics in cross strip semiconductor detectors". In: *Nuclear Instruments and Methods in Physics Research Section A: Accelerators, Spectrometers, Detectors and Associated Equipment* 1052 (2023), p. 168310. ISSN: 0168-9002. DOI: <https://doi.org/10.1016/j.nima.2023.168310>.
- [49] Nicolas Abgrall et al. "The M AJORANA D EMONSTRATOR Neutrinoless Double-Beta Decay Experiment". In: *Advances in High Energy Physics* 2014 (2014).
- [50] C Cuesta, Majorana Collaboration, et al. "Background model for the Majorana Demonstrator". In: *Journal of Physics: Conference Series*. Vol. 888. 1. IOP Publishing, 2017, p. 012240.
- [51] H. Spieler. *Semiconductor Detector Systems*. Oxford: Clarendon Press, 2005.
- [52] GERDA Collaboration et al. "Improvement of the energy resolution via an optimized digital signal processing in GERDA Phase I". In: *European Physical Journal C* 75.255 (2015). DOI: 10.1140/epjc/s10052-015-3409-6.
- [53] C. Jacoboni et al. "Electron drift velocity and diffusivity in germanium". In: *Phys. Rev. B* 24 (2 July 1981), pp. 1014–1026. DOI: 10.1103/PhysRevB.24.1014.
- [54] R. Henning. *PIRE GEMADARC Course on Concepts of Detector Electronics - Lecture Notes*. Accessed: 2024-07-21. 2020. URL: <http://pire.gemadarc.org/education/school20/#electronics>.
- [55] P. Barton et al. "Ultra-low noise mechanically cooled germanium detector". In: *Nuclear Instruments and Methods in Physics Research Section A: Accelerators, Spectrometers, Detectors and Associated Equipment* 812 (2016), pp. 17–23. ISSN: 0168-9002. DOI: <https://doi.org/10.1016/j.nima.2015.12.031>.
- [56] V Radeka. "Low-Noise Techniques in Detectors". In: *Annual Review of Nuclear and Particle Science* 38. Volume 38, 1988 (1988), pp. 217–277. ISSN: 1545-4134. DOI: <https://doi.org/10.1146/annurev.ns.38.120188.001245>.

- [57] Giovanni Benato. “Data Reconstruction and Analysis for the GERDA experiment”. PhD thesis. University of Zurich, 2015.
- [58] Michael Willers. “Signal Readout Electronics for LEGEND-200”. In: *J. Phys. Conf. Ser.* 1468.1 (2020). Ed. by Masayuki Nakahata, p. 012113. doi: 10.1088/1742-6596/1468/1/012113. arXiv: 1911.05847 [physics.ins-det].
- [59] N Abgrall et al. “The Majorana low-noise low-background front-end electronics”. In: *Physics Procedia* 61 (2015), pp. 654–657.
- [60] Stefano Riboldi, Alberto Pullia, and Carla Cattadori. “Improvement of the “CC2” charge sensitive preamplifier for the GERDA phase II experiment”. In: *2012 IEEE Nuclear Science Symposium and Medical Imaging Conference Record (NSS/MIC)*. IEEE, 2012, pp. 782–785.
- [61] P. Barton et al. “Ultra-low noise mechanically cooled germanium detector”. In: *Nuclear Instruments and Methods in Physics Research Section A: Accelerators, Spectrometers, Detectors and Associated Equipment* 812 (2016), pp. 17–23. issn: 0168-9002. doi: <https://doi.org/10.1016/j.nima.2015.12.031>.
- [62] Paolo Carniti. “Electronic Instrumentations for High Energy Particle Physics and Neutrino Physics”. In: *arXiv preprint arXiv:1808.10193* (2018).
- [63] Filippo Schembari. “Development and characterization of a low noise multichannel readout asic for X and γ -ray spectroscopy applications”. In: (2016).
- [64] C Fiorini and Matteo Porro. “Integrated RC cell for time-invariant shaping amplifiers”. In: *IEEE Transactions on nuclear science* 51.5 (2004), pp. 1953–1960.
- [65] *LegendSpecFits.jl - LEGEND tools to fit spectra*. URL: <https://github.com/legend-exp/LegendSpecFits.jl>.